ORIGINAL PAPER

Modeling, simulation, and optimization of geothermal energy production from hot sedimentary aquifers

Laura Blank[1] · Ernesto Meneses Rioseco[2,3] · Alfonso Caiazzo[1] (ID) · Ulrich Wilbrandt[1]

Abstract

Geothermal district heating development has been gaining momentum in Europe with numerous deep geothermal installations and projects currently under development. With the increasing density of geothermal wells, questions related to the optimal and sustainable reservoir exploitation become more and more important. A quantitative understanding of the complex thermo-hydraulic interaction between tightly deployed geothermal wells in heterogeneous temperature and permeability fields is key for a maximum sustainable use of geothermal resources. Motivated by the geological settings of the Upper Jurassic aquifer in the Greater Munich region, we develop a computational model based on finite element analysis and gradient-free optimization to simulate groundwater flow and heat transport in hot sedimentary aquifers, and numerically investigate the optimal positioning and spacing of multi-well systems. Based on our numerical simulations, net energy production from deep geothermal reservoirs in sedimentary basins by smart geothermal multi-well arrangements provides significant amounts of energy to meet heat demand in highly urbanized regions. Our results show that taking into account heterogeneous permeability structures and a variable reservoir temperature may drastically affect the results in the optimal configuration. We demonstrate that the proposed numerical framework is able to efficiently handle generic geometrical and geological configurations, and can be thus flexibly used in the context of multi-variable optimization problems. Hence, this numerical framework can be used to assess the extractable geothermal energy from heterogeneous deep geothermal reservoirs by the optimized deployment of smart multi-well systems.

1 Introduction

Stored heat in the subsurface in a variety of geological settings is recognized as geothermal energy and constitutes a renewable resource that can be sustainably and environmentally friendly recovered by diverse utilization concepts [1, 2].

Among the many possible geothermal energy uses, geothermal district heating development has been gaining momentum in Europe with a significant installed capacity and numerous projects currently under development [3–8]. In particular, the Greater Munich region in Germany

shows one of the most dynamic developments [9–12], where numerous deep geothermal facilities have gone into operation in the last two decades, meeting the heat demand of several villages and neighborhoods of Munich (see also Fig. 1).

Research projects such as GRAME [14, 15] and GEO-maRE[1] are prominent examples of efforts taken to facilitate the German energy transition by substantially contributing to the decarbonization of district heating networks in large cities. They clearly evidence that considerable heat demand together with significant accessible geothermal resources and an economic, technological, and political commitment to the transition to renewal energy are key ingredients for a sustainable and decarbonized district heating development. Large companies such as the municipal energy supplier of Munich (Stadtwerke München—SWM) envision that the

---

✉ Alfonso Caiazzo
   Alfonso.Caiazzo@wias-berlin.de

Extended author information available on the last page of the article.

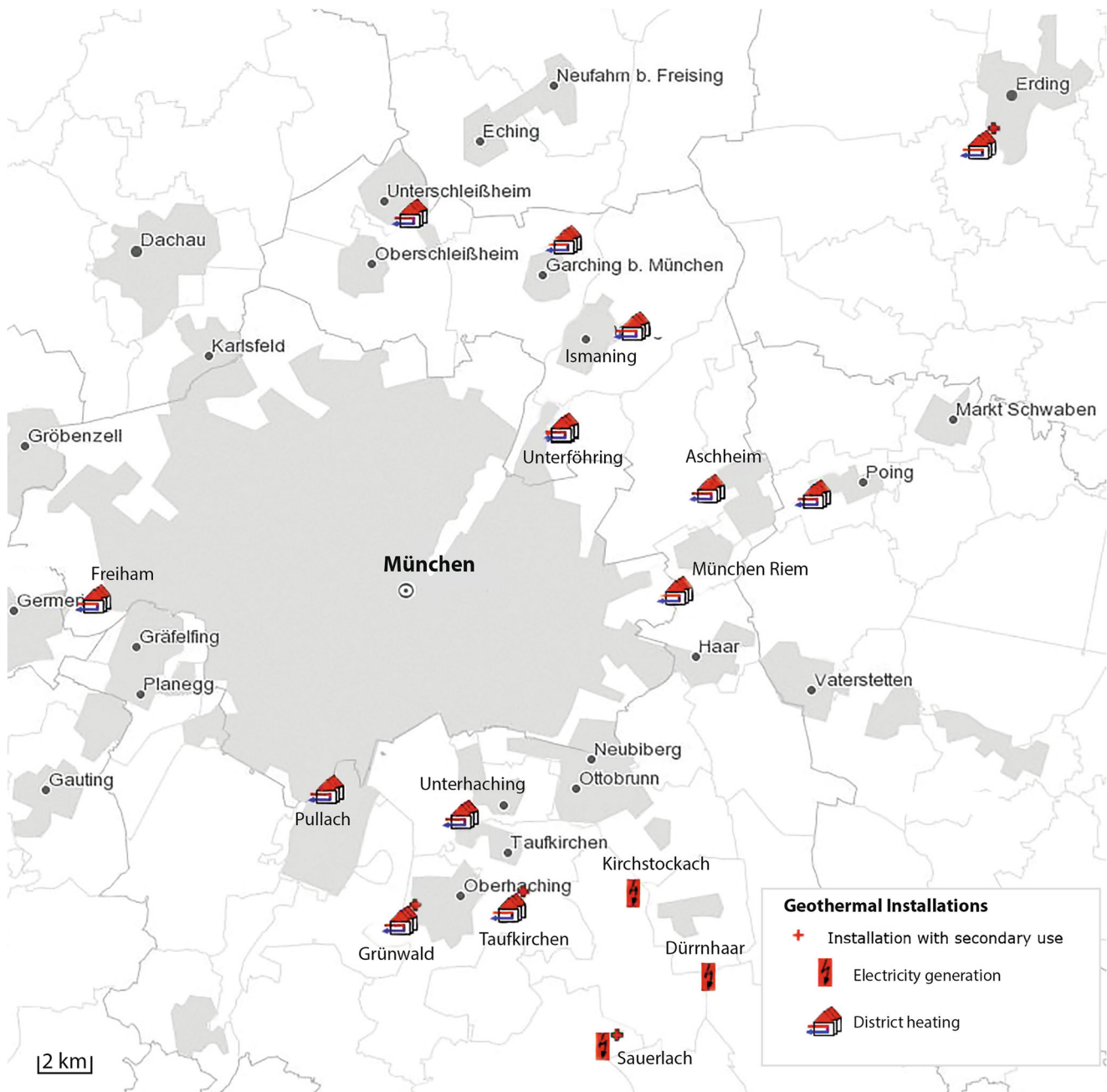[1] See https://www.enargus.de/pub/ bscw.cgi/.

Fig. 1 Geothermal facilities that have been under operation for several years in the Greater Munich region. Note that both electricity and heat are being produced. Each geothermal plant consists of a doublet or a triplet. In the case of the Unterföhring geothermal plant, two doublets are implemented. This picture has been obtained from the German geothermal information system GeotIS (http://www.geotis.de, June 2019 [9, 10, 13]) and has been subsequently modified

heat demand of the city of Munich should be met by 2040 completely by renewable energy [14, 15]. To accomplish this, 400MW$_{th}$ should be provided by geothermal district heating, which means that deep geothermal energy shall contribute the most to the heat transition.

With the increasing density of geothermal wells during the life cycle of a geothermal field development, questions related to the optimal and sustainable reservoir exploitation become more and more important [4, 11, 16–19].

For sustainability, the future deployment of wells has to be chosen in such a way that negative interference with existing neighboring wells is avoided while their positive interference is promoted. In addition, the placement and spacing of new geothermal wells and their operational

schemes have to be carefully selected depending on the geometric dimensions of geothermal concession fields to avoid thermo-hydraulic encroachment. This refers specifically to the spatio-temporal evolution of the cooling front emanating from the injection wells, which is mainly controlled by the permeability structure, thickness of the aquifer, exploitation scheme (injection and production rates), and a possible thermo-hydraulic interaction with wells in the vicinity.

In the last decades, the usage of optimization algorithms to optimize well patterns has gained increasing popularity for a sustainable reservoir management in the hydrocarbon industry (see, e.g., [20–23]). In contrast to geothermal exploitation concepts, the geometric well configurations normally considered in the oil and gas industry are intended to optimize the oil and gas recovery from hydrocarbon-bearing formations by efficiently sweeping the hydrocarbons towards the production wells through fluid injection. In the geothermal context, however, other aspects drive the use of optimized multi-well configurations. In particular, in highly populated urban cities with a lack of space for numerous geothermal drilling sites and a huge heat demand, specific arrangements of multiple geothermal wells are of great interest. In addition to the search of an optimal geothermal site depending on the site-specific geothermal and hydrogeological conditions, the optimized multi-well configuration, spacing, and operational schemes for the economic utilization time span are among the key questions, which have not been extensively investigated yet. Concerning the economic lifetime of a geothermal plant based on open loops, special attention is paid to the thermal breakthrough and possible thermal short circuits [24–29].

Finding the optimal set of decisions among different options is a multi-variable optimization problem. Important factors include the number and type of wells, well locations, production and injection constraints, and economic factors like operating costs. The optimization task is even more challenging due to geological uncertainties associated with reservoir petrophysical parameters (e.g., thermal conductivity, porosity, and permeability) varying over a wide range of values and heterogeneities of subsurface domains (e.g., temperature, pressure, and permeability fields).

As reliable and quantitative tools, mathematical modeling and computer simulation of geothermal reservoir processes, especially in connection with optimization problems related to multi-well configurations and well patterns, have received considerable attention in the last years. Several recent works employ diverse numerical methods (e.g., finite difference, finite volume, or finite element) as well as different approaches to solve related optimization problems. Among others, [11] proposed a thermo-hydraulic model

of the geothermal Upper Jurassic aquifer in the Munich region, based on a finite element method, in order to forecast long-term temperature and pressure fields in multi-well configurations. Based on this model, preliminary aspects of the optimal design problem were recently investigated and presented in [16, 17], numerically confirming advantages of doublet arrays compared with a single doublet. Modeling of hot sedimentary aquifers was also investigated in [19] and [30], taking into account the impact of sandstone reservoir heterogeneities on geothermal doublets production performance.

Reservoir lifetimes for doublets in hot sedimentary aquifers were recently studied in [31, 32], and in [18], including lattice-type configurations and sizes of geothermal concession fields. Very recently, automatic optimization methods based on genetic algorithms have been proposed in [33, 34], considering heterogeneous reservoirs but limited to Cartesian meshes. Further, in [35] a gridblock-based optimization strategy with a stochastic optimization is tested.

Great efforts have been made also in the development of software frameworks for the simulation of groundwater flow and heat and mass transport in porous and fractured geologic media. Among the most popular tools, there are several commercial packages as FEFLOW developed by DHI-WASY GmbH, COMSOL Multiphysics developed by COMSOL, MOOSE developed by the Idaho National Laboratory, TOUGH2/TOUGHREACT developed by the Earth Science Division of the Lawrence Berkeley National Laboratory, and FLUENT developed by ANSYS Inc., to mention a few.

Commercial software can be used by practitioners without requiring particular knowledge about the details of the numerical discretizations. However, this aspect makes it relatively difficult to further develop these packages for user-specific purposes and/or to tackle new research questions. The multi-physical nature of geothermal reservoirs requires collaborative and interdisciplinary research, combining the most recent advantages in mathematical modeling, simulation, computational geometry, and, as in the case of this paper, optimization. This is one of the reasons that motivated, especially in latest years, the initiation of several open-source projects for collaborative software platforms. In the context of groundwater flow modeling, notable projects include Open Porous Media[2], OpenGeoSys[3], DuMuX[4], MODFLOW [36], and the Python package PorePy [37]. Other widely used packages developed for a broader range of applications include FEniCS

---

[2]https://opm-project.org/.

[3]https://opengeosys.org.

[4]https://dumux.org.

[38], DUNE [39], or deal.II [40]. The interested reader is referred to [41] for an extensive review of open-source packages as well as for a detailed discussion on the benefit of open-source platforms.

We present a numerical model based on the finite element approximation of a general Darcy–Brinkman problem, suitable for a wide range of physical parameters, including larger permeabilities, coupled to a finite element solver for the temperature field. The model is based on the mixed (or dual) formulation of the groundwater flow problem. Unlike the simpler (and widely used in the context of geothermal modeling, e.g., [42]) primal formulation, in which the numerical solution is computed only for the pressure, in the mixed form, the problem is solved for both velocity and pressure. At the expense of a slightly higher computational complexity, the mixed form allows to compute more regular velocity fields. Moreover, we use the mixed formulation in combination with a non-matching (immersed) method to account for the boundary conditions at the wells as *singular* forces. An analogous approach has been also used in several previous works (e.g., [18, 42]), but only for the primal formulation and restricted to the case of point-associated wells located at mesh vertices. In this paper, we show that based on the mixed Darcy–Brinkman problem, the imposition of singular sources/sinks of mass can be decoupled from the spatial discretization. From the practical viewpoint, this is a major advantage especially when the simulation of numerous scenarios of multiple well arrangements is intended, as it does not require the regeneration of the computational mesh.

In the context of sustainable and optimized geothermal energy production by selected smart multi-well patterns, the scope of this work is to present a fit-for-purpose computational model of coupled groundwater flow and heat transport, integrating an optimization algorithm with diverse geothermal multi-well arrangements. The numerical framework includes the development of a mathematical model that enables a quantitative assessment of maximum sustainable production of geothermal energy, taking into account the underground temperature field, thermal and hydraulic property distributions, and thermo-hydraulic interactions between neighboring wells. Heat transport mainly by advective and diffusive processes in porous, fractured, and karstified reservoirs in the framework of the equivalent porous medium (EPM) approach is computed in this work (see, e.g., [43]). This choice is motivated by the results and by the observations—among others—of [11, 44], who gathered ample, real data of the Upper Jurassic carbonates in the Munich region at an intermediate- and a regional-scale and conducted an extensive characterization of the Upper Jurassic carbonates. Although we focus

on similar reservoir conditions as found in the Upper Jurassic carbonates in the Munich region, the methodology developed here can be applied to any hot sedimentary aquifer.

Regarding the optimization of geothermal energy extraction, the main goal of this work is to describe and quantify the thermo-hydraulic effects on the placement and spacing of different geothermal multi-well patterns with varying geothermal and hydrogeological conditions. Therefore, we concentrate on parameters that specify the arrangement of the wells. However, the approach can be extended to an arbitrary number of control variables (e.g., injection and production flow rates, injection temperatures). These problems as well as the use of more efficient optimization methods are subjects of ongoing research. One of the important capabilities of the optimization method used in this work is to search in narrow and tight spaces through the entire geothermal reservoir to select optimal placements of multi-well configurations and spacing parameters. This relates to maximizing the net energy production during the life cycle of geothermal reservoir development. Advantages and disadvantages of the utilization of different multi-well configurations are discussed.

We restrict in this work to a fit-for-purpose numerical modeling of geothermal reservoirs in two dimensions, studying diverse scenarios of multiple geothermal well arrangements in varying geothermal and hydrogeological conditions in a reasonable time frame.

A further motivation of our work is the assessment of open-source tools to tackle the optimization problem. The above described numerical method has been implemented in the open-source finite element library ParMooN, developed at the WIAS [45]. The optimization problem is solved with a gradient-free, global optimization algorithm, which has been implemented within the open-source library NLopt. In particular, we perform a detailed validation of the numerical schemes against reference and analytical solutions, investigating the sensitivity with respect to the discretization parameters (spatial and temporal mesh sizes) and the boundary conditions.

The rest of the paper is organized as follows. Section 2 aims at introducing the geothermal and hydrogeological settings that are employed to determine the details of the simulations. In Section 3, the main ingredients of our computational framework are presented: the groundwater flow model, the heat transport model, the optimization algorithm, and the corresponding numerical schemes. In Section 4, we describe the different scenarios which are investigated computationally, while Section 5 is dedicated to the main results of our numerical simulations. Conclusions are drawn in Section 6.

2 Geothermal and hydrogeological setting

The thermo-hydraulics of geothermal reservoirs is based on the combination of a geothermal and a hydrogeological model. Therefore, considerable effort should be taken to characterize both the geothermal and hydrogeological conditions normally encountered in hot sedimentary aquifers.

2.1 Temperature distribution and geothermal context

Detailed knowledge on underground temperature distribution is crucially important for the assessment of geothermal energy potential. The temperature field in hot sedimentary aquifers mainly found in intracratonic or foreland basin geothermal play types is predominantly driven by natural heat conduction [2, 46, 47]. A near average heat flow is recognized as the heat source in deep-seated aquifers in conduction-dominated hydrothermal systems [2, 48–52].

Roughly, an average geothermal gradient of around 30°C per kilometer is established in these geothermal play types. Ample data on temperature measurements has been gathered by the hydrocarbon industry through oil and gas exploration in sedimentary basins, and subsequently corrected and put into a geothermal context [9, 10, 53]. Moreover, geothermal exploration has contributed to the

understanding of subsurface temperature distribution in sedimentary basins [54–56]. In addition, thermal properties of different reservoir rocks, i.e., thermal conductivity, volumetric heat capacity, and thermal diffusivity, have been measured and described in, e.g., [57–64].

Since the South German Molasse Basin and in particular the Bavarian Molasse Basin is one of the best studied foreland basins and the only geothermally developed foreland basin worldwide [2, 11, 65–67], extensive geoscientific data has been collected. Especially, the porous, fractured, and karstified Upper Jurassic carbonates of the South German Molasse Basin are recognized as the most important hydrothermal reservoir for deep geothermal energy utilization in Germany and Middle Europe [11, 67–72].

Due to this remarkable development and the related increasing concentration of geothermal wells, we focus in this work on similar geothermal and hydrogeological conditions as encountered in the Upper Jurassic (Malm) aquifer in the Greater Munich region. However, as mentioned earlier, the methodology developed in this work can be applied to other low-enthalpy geothermal reservoirs that classify as hot sedimentary aquifers. Figure 2 displays the temperature distribution at the top Upper Jurassic formation in the Greater Munich region. Due to the down-bending of the lithosphere from North to Southeast towards the Alpine Orogenic Belt, a laterally and vertically varying
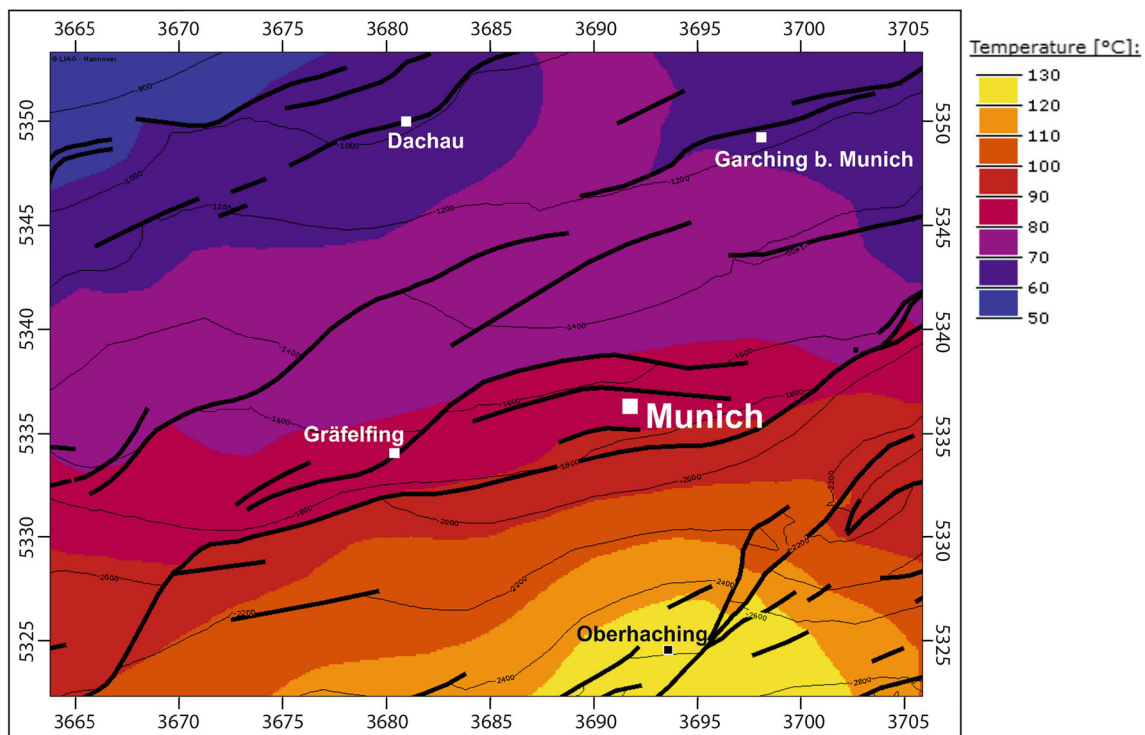

Fig. 2 Temperature distribution at the top Upper Jurassic (Malm) formation in the Bavarian Molasse Basin. Note the temperature range in southern urban Munich between 80 and 100°C. Black thick lines display major faults that cross the Malm aquifer. This picture is based on the compiled database at the LIAG and stems from GeotIS [9, 13]. It has been modified

temperature field reigns in the Upper Jurassic aquifer (see Figs. 2 and 3). Based on this fact, some of the scenarios considered for the well placement optimization in this work include the effect of a laterally varying temperature field. Furthermore, a present-day average surface heat flow of around 65 mW/m^2 and an average surface temperature of approximately 10°C have been documented in the literature for Germany [7, 53, 73–75]. In particular, in the Bavarian Molasse Basin, the surface heat flow varies between 60 and 80mW/m^2 [76].

2.2 Permeability structure and hydrogeological background

When it comes to the hydraulics of groundwater in hot sedimentary aquifers, one-phase, liquid-dominated, laminar fluid dynamics is normally considered in confined and saturated reservoir conditions. Besides, fluid flow in clastic and carbonate reservoirs occurs in many different aquifer types such as porous, fractured, and karstified aquifers, [77, 78]. Geologically modeling the heterogeneities and
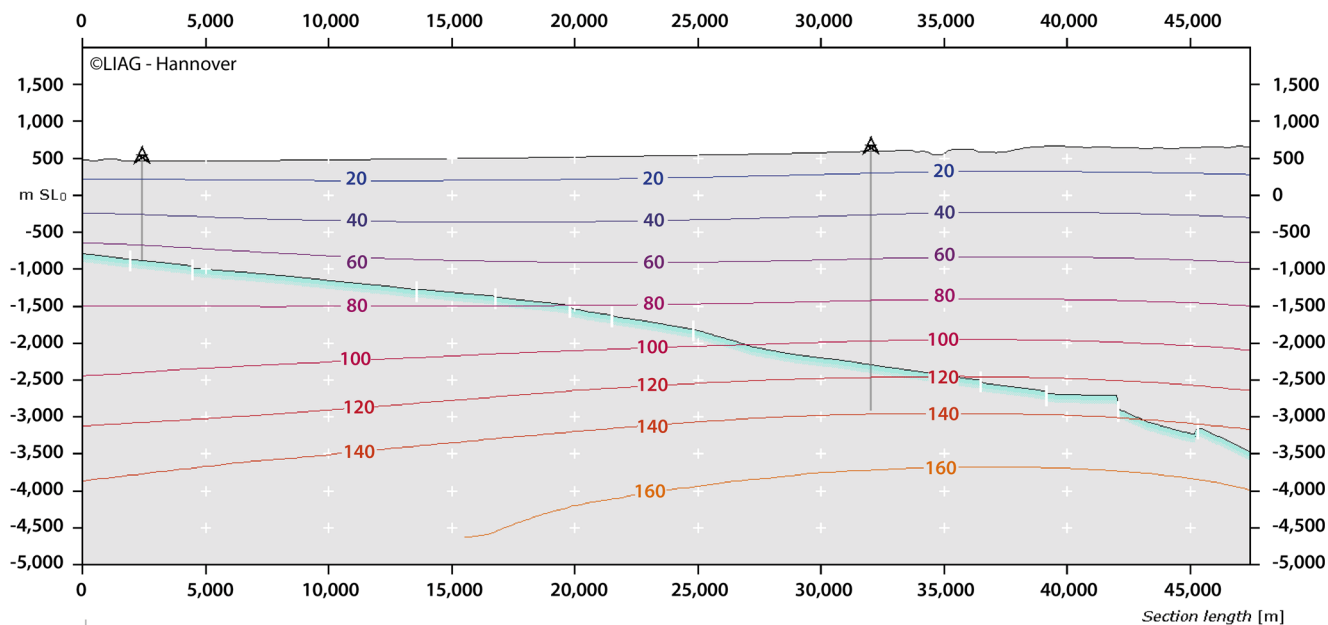

Fig. 3 Vertical profile (top picture) of the temperature distribution along a North-South oriented line that crosses the city of Munich (from left to right corresponds to the profile from A to A' in the bottom picture). The Upper Jurassic formation is depicted in blue greenish color.

Note the threefold vertical exaggeration and the southwards declination of the Upper Jurassic formation (towards the Alps). This picture has been built with GeotIS [9, 13]

anisotropies encountered in such aquifers remains an ongoing effort [79].

Since permeability is the main control on fluid flow and consequently on heat and mass transport in aquifers, the characterization of the permeability structure of hot sedimentary aquifers is a key ingredient for a sound assessment of geothermal reservoir performance. Concerning reservoir quality of deep sandstone and carbonate aquifers encountered in foreland basin and intracratonic basin geothermal play types in Europe, ample data in terms of porosity and permeability parameter ranges has been published (e.g., [80–84]). In particular, a large set of hydraulic conductivity and permeability values has been documented in [11, 85, 86].

The regional and local natural groundwater flow in hot sedimentary aquifers is mainly dominated by the existing hydraulic gradient and the permeability structure of the aquifer at hand. It is in general overprinted by the relatively high flow rates, imposed by the permanent production and injection rates used for heat extraction in numerous multi-well arrangements [66]. In the case of the Upper Jurassic aquifer in the South German Molasse Basin, numerous pump and injection tests have been analyzed in, e.g., [44, 85]. Particularly concerning the hydraulic activity of fault damage zones, it is still debated for the case of the Upper Jurassic aquifer in the Bavarian Molasse Basin whether linear (controlled by the fault damage zone permeability), radial (controlled by the matrix permeability), or bilinear (combined linear flow in perpendicular directions in both the fault and the matrix) is the dominant flow regime, [44, 87]. However, most of the related, published studies claim that the majority of the hydraulically tested fault damage zones of the Upper Jurassic aquifer in the Greater Munich region shows a rather radial flow regime [44]. Fundamentally, the ratio between matrix and fault damage zone permeability controls what kind of flow regime predominates, whether linear, radial, or bilinear flow.

Recently, a multidisciplinary geothermal reservoir characterization of the Upper Jurassic aquifer (Malm) in the Greater Munich region has been conducted in [11]. The combination of a variety of geophysical and geological data led to reliable hydraulic reservoir properties and sound knowledge of the permeability structure. Regional and local structural-geological elements as well as facies distribution were integrated in a geothermal reservoir model. Carbonate reservoirs are distinguished by their highly variable permeability structure. The work of [11] presents a wide range of hydraulic conductivity values in the order of 10^{-4} to 10^{-9} m/s. The incorporation of outcrop data, main inflow zones data in geothermal boreholes, multiple logging data of several geothermal and hydrocarbon wells in the region, and pump and injection test data led to a simplified hydrostratigraphic standard profile of the Upper Jurassic aquifer

in the Greater Munich region, presented in [11]. Based on these reservoir characterization and modeling results, some scenarios with laterally varying hydraulic conductivity (or the respective permeability), which is caused by the presence of different carbonate facies or by fault damage zones, are considered in the present work in order to assess its effect on the well placement optimization. Figure 4 shows the overall hydraulic conductivity of the Upper Jurassic geothermal reservoir, which decreases from North to Southwest as the Malm aquifer deepens towards the Alpine orogenic front (see also Fig. 3). Besides, the overriding cretaceuos and tertiary layers and the underlying crystalline basement, which delimit the Malm aquifer, are considered as hydraulically non-conductive (aquitards). Based on existing drinking water wells and thermal water boreholes, an equipotential line map for the thermal water in the Malm of the Southern German Molasse Basin was built by [88], but the currently ongoing discussion suggests a revision of the normalization procedure in the identification of groundwater potential. Due to the still large uncertainties with regard to the current groundwater flow regime in the Malm aquifer and the existing, comparatively low hydraulic gradient, a constant underlying pressure field can alternatively be considered for the thermo-hydraulic modeling.

3 Mathematical model

The mathematical model developed in this work consists of two components: Firstly, a fluid flow model for a confined and saturated aquifer, which is assumed to be predominantly composed of consolidated sedimentary material as, e.g., sandstones and/or carbonates. Secondly, an advection-diffusion model for the temperature distribution.

These two problems are sequentially coupled, i.e., the velocity solution of the Darcy–Brinkman problem determines the advective field used in the differential equation describing the temperature evolution.

Based on the geothermal and hydrogeological setting described in Section 2, the model is build upon the following assumptions:

(A1) We consider an aquifer confined by overriding and underlying aquitards. As a consequence, fluid flow through the top and bottom boundaries of the reservoir is neglected. Moreover, assuming that the vertical dimension is much smaller than the horizontal characteristic size, we neglect the effect of gravitational forces (two-dimensional approximation).

(A2) Groundwater flow is modeled by the Brinkman equations [89]. Compared with the frequently used Darcy model, an additional term accounting for
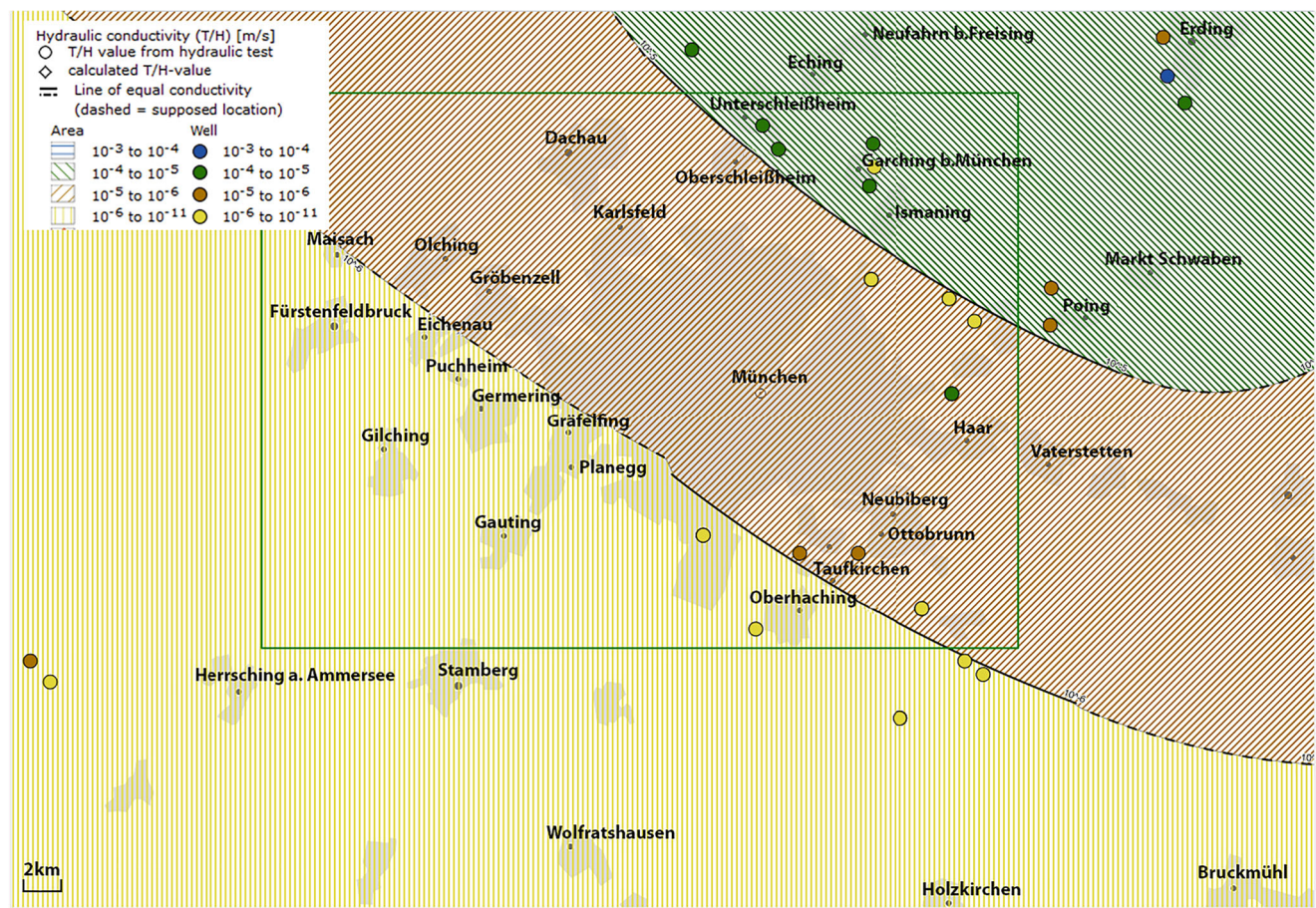
Fig. 4 Regional hydraulic conductivity trend for the Upper Jurassic formation in the Greater Munich region. Shaded areas show urban regions. The green rectangle displays the area represented in Fig. 2. Note the regional trend of decreasing hydraulic conductivity in the southwestern direction. This picture is based on the compiled database at the LIAG and results from the work done by [44]. It originates from GeotIS [9, 13] and has been modified

viscous stresses is present in the momentum balance equation. This allows to go beyond the range of validity of Darcy's law towards regimes of higher permeability, which is particularly interesting for vuggy porous media resulting from, e.g., karstification and highly damaged zones in faulted domains (see, e.g., [90, 91]).

(A3) Steady-state flow of a single-phase, incompressible, Newtonian fluid in an isotropic, saturated, non-deformable aquifer, taking into account the equivalent porous medium approach for possibly karstified and fractured domains that exhibit high permeabilities.

(A4) The dependence of fluid viscosity and fluid density on temperature is neglected for the range of temperatures considered.

(A5) The heat transport model is confined to the aquifer under investigation, i.e., heating or cooling due to the temperature of the aquitards is neglected.

(A6) The thermal dispersion is in most cases dominated by the longitudinal contribution, such that the transversal dispersion is neglected in the following. Further, we consider a temperature-independent volumetric heat capacity and thermal conductivity.

3.1 Aquifer model

The domain of interest is an aquifer of constant thickness H (m) with rectangular base of diameter L (m), with $H \ll L$. Each well is modeled as a cylindrical borehole $w_{3D}^{(\star)}$, see Fig. 5 (top).

In the horizontal direction, the fluid is allowed to permeate through the medium boundaries, while eventual phenomena in the vertical direction are neglected. Hence, for the remainder of this work we focus on a 2D slice, parallel to the confining planes, as illustrated in Fig. 5 (bottom). Let $\Omega \subset \mathbb{R}^2$ be the spatial domain under consideration. We denote by $w^{(\star)}$ the 2D slice of the
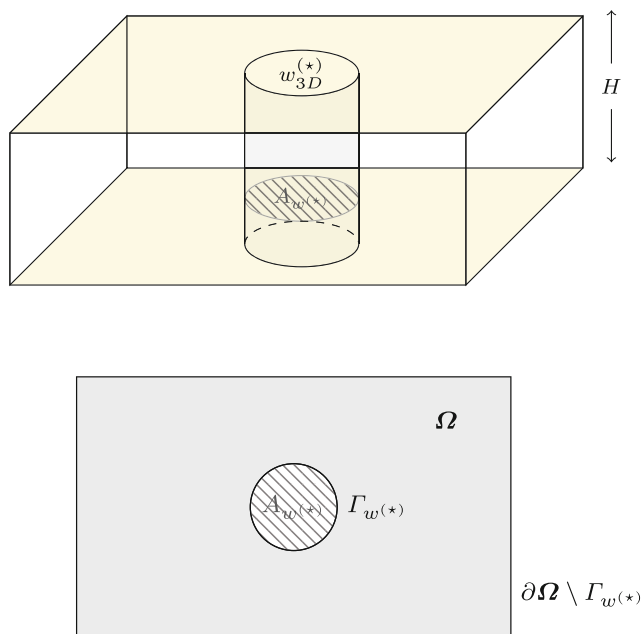
Fig. 5 Top: Schematic 3D model of an aquifer, fully penetrated by a single cylindrical well $w_{3D}^{(\star)}$. Top and bottom of the aquifer (yellow) are impermeable for fluid. Bottom: A horizontal cross-section

well with cross-sectional area $A_{w^{(\star)}}$ (m^2) and by $\Gamma_{w^{(\star)}}$ the boundary of $w^{(\star)}$.

Later on we will distinguish between production wells and injection wells by using the respective symbol $(\star) \in \{\text{prod, inj}\}$. The same notation is adopted for other quantities that are associated with production and injection wells, respectively.

3.2 Groundwater flow

This section focuses on the mathematical modeling, based on the stationary Brinkman (or Darcy–Brinkman) equations [89], combined with an immersed method to take into account the effect of production and injection wells.

3.2.1 The Darcy–Brinkman model

Assuming conservation of mass and (linear) momentum, we consider the following system of partial differential equations [89]:

$$-\mu_{\text{eff}} \Delta \boldsymbol{u} + \nabla p + \sigma \boldsymbol{u} = \mathbf{f} \qquad \text{in } \boldsymbol{\Omega}, \tag{1a}$$

$$\nabla \cdot \boldsymbol{u} = g \qquad \text{in } \boldsymbol{\Omega}, \tag{1b}$$

where $\boldsymbol{u} : \boldsymbol{\Omega} \to \mathbb{R}^2$ (m/s) is the velocity field, $p : \boldsymbol{\Omega} \to \mathbb{R}$ (Pa) is the pressure field, μ_{eff} (kg/m s) denotes the effective viscosity, and $\sigma := \mu K^{-1}$, i.e., the fraction of fluid viscosity μ (kg/m s) and permeability K (m^2) of the porous medium. Moreover, $\boldsymbol{f}$ (N/m^3) models external volume forces, while g (s^{-1}) takes into account sources or

sinks of mass. For the considered two-dimensional case, external volume forces as well as mass sources within the aquifer vanish in Eq. 1a–Eq. 1b.

Problem 1 is completed with the following boundary conditions. Along each well boundary, a constant velocity magnitude $U_{w^{(\star)}}$ (m/s) directed normally to the well boundary is assumed, yielding the Dirichlet boundary conditions

$$\boldsymbol{u} = \pm U_{w^{(\star)}} \boldsymbol{n}_{w^{(\star)}} \qquad \text{on } \Gamma_{w^{(\star)}}, \ \forall w^{(\star)}, \tag{1c}$$

where $\boldsymbol{n}_{w^{(\star)}}$ is pointing from the well into the porous medium (inner unit normal vector). Positive and negative signs in front of $U_{w^{(\star)}}$ shall be used to represent flow into (injection) or out of (production) the aquifer with respect to the well, respectively. The value of the in-/outflow velocity, $U_{w^{(\star)}}$ in Eq. 1c, depends on the prescribed injection and production rate, respectively, and the thickness H (m) of the aquifer (see Subsection 3.1). Let us assume that the fluid is injected or extracted uniformly along the vertical direction of the generic cylindrical well $w_{3D}^{(\star)}$ with flow rate $Q_{w_{3D}}^{(\star)}$ (m^3/s). Then, the magnitude of the velocity along the well boundary for the two-dimensional problem is given by

$$U_{w^{(\star)}} = \frac{Q_{w_{3D}}^{(\star)}}{2\pi r_{w^{(\star)}} H} \qquad \text{on } \Gamma_{w^{(\star)}}, \tag{2}$$

with $r_{w^{(\star)}}$ (m) denoting the radius of the well.

Neumann boundary conditions are imposed on the outer boundary, setting the external pressure equal to a given function, i.e.,

$$(\mu_{\text{eff}} \nabla \boldsymbol{u} - p\mathbb{I}) \cdot \boldsymbol{n} = P\boldsymbol{n} \qquad \text{on } \partial\boldsymbol{\Omega} \setminus \bigcup_{w^{(\star)}} \Gamma_{w^{(\star)}}, \tag{3}$$

where $\boldsymbol{n}$ stands for the outer unit normal vector.

A constant pressure (set to $P = 0$ Pa) at the aquifer boundaries is used in the computations described in Section 5, assuming that natural flow in the geothermal reservoir can be neglected in comparison with the flow induced by operating injection and production wells (see Section 2).

Remark 1 (Darcy versus Brinkman formulation) If inertia forces are small compared with damping/resistive forces, the system Eq. 1a–Eq. 1b naturally reduces to the classical Darcy model. In case the targeted reservoir region contains hydraulically conductive fractures, fault damage zones, or karstified domains, high permeabilities might lead to groundwater flow regimes, where the interaction of fluid particles (inertial forces) becomes relevant, making the use of the more general Brinkman model (Eq. 1) necessary. As explained in further detail in Section 3.4, the numerical method designed and employed to approximately solve Eq. 1 is robust with respect to the physical parameters (μ_{eff}

and σ), i.e., it can be used in a similar manner for the Darcy limit as well.

3.2.2 Model of wells through singular forces

In deep geothermal applications, the radii of the cylindrical wells, e.g., 0.1 m in [92], are much smaller than the scale of the domain (several kilometers). The presence of this wide range of spatial scales might considerably increase the computational complexity if the computational mesh is required to accurately resolve the well boundary. In order to circumvent this issue, we employ the so-called *immersed boundary method* [93], which is based on considering an extended domain, which includes the well regions and describes the limit case when the well radii tend to zero. The wells are then described as singular forces defined in single points (the well centers).

Accordingly, we consider a flow problem defined over an extended domain $\widehat{\boldsymbol{\Omega}} := \boldsymbol{\Omega} \cup \left(\bigcup_{w^{(\star)}} w^{(\star)} \right)$ (see Fig. 5 bottom), where the presence of wells is taken into account assuming that the divergence of the velocity field vanishes everywhere except for the centers of injection and production wells. This is modeled via singular sources (or sinks) of mass in Eq. 1b, i.e.,

$$\nabla \cdot \boldsymbol{u} = \sum_{l=1}^{N^{\text{inj}}+N^{\text{prod}}} g_{w_l^{(\star)}} \delta_{w_l^{(\star)}}, \quad \text{in } \widehat{\boldsymbol{\Omega}}. \tag{4}$$

Here, N^{inj} is the number of injection wells, N^{prod} refers to the number of production wells, $\delta_{w_l^{(\star)}}$ denotes the Dirac delta distribution with respect to the well center, and $g_{w_l^{(\star)}}$ are proper constants which depend on the prescribed injection or production rates, respectively.

Let us consider the case of a single well $w^{(\star)}$. In order to determine the singular force $g_{w^{(\star)}}$, we note that the solution of the problem with the original boundary condition Eq. 1c satisfies

$$\int_{w^{(\star)}} \nabla \cdot \boldsymbol{u} = \int_{\Gamma_{w^{(\star)}}} \boldsymbol{u} \cdot \boldsymbol{n}_{w^{(\star)}} = \pm U_{w^{(\star)}} 2\pi r_{w^{(\star)}} = \pm \frac{Q_{w_{3D}}^{(\star)}}{H}, \tag{5}$$

where we have used the Gaussian theorem, the boundary condition Eq. 1c, the fact that $|\Gamma_{w^{(\star)}}| = 2\pi r_{w^{(\star)}}$, and the expression Eq. 2 for $U_{w^{(\star)}}$. On the other hand, integrating Eq. 4 over the boundary of the circle $w^{(\star)}$, using Eq. 5, the fact that $g_{w^{(\star)}}$ is constant, and the property $\int_{w^{(\star)}} \delta_{w^{(\star)}} = 1$ of the Dirac delta distribution, we obtain

$$g_{w^{(\star)}} = \int_{w^{(\star)}} g_{w^{(\star)}} \delta_{w^{(\star)}} = \int_{w^{(\star)}} \nabla \cdot \boldsymbol{u} = \pm \frac{Q_{w_{3D}}^{(\star)}}{H}. \tag{6}$$

Hence, we replace the flow problem Eq. 1 with a problem defined on $\widehat{\boldsymbol{\Omega}}$. Instead of the Dirichlet boundary condition

Eq. 1c, the prescribed flow rate is then imposed via the modified mass conservation Eq. 4.

One of the main advantages from the practical point of view is that the immersed method allows for a coarser spatial discretization, thus reducing the computational effort for the numerical simulation. Immersed methods have been previously used in the context of simulation of perfusion within biological tissues [94, 95] as well as in [42] for the simulation of groundwater flow. In this latter case, however, the singular problem was derived from the primal Darcy formulation, instead of the mixed general Darcy–Brinkman problem.

At the discrete level, there are different approaches to include the singular forces in Eq. 4 in a numerical method. One possibility is to assume that the points, where the singular sources and sinks are defined, coincide with vertices (or edges in 3D) of the considered computational mesh (see, e.g., [42, 94]). This choice, however, strongly links the singular sources to the mesh generation.

We adopt a *non-matching* approach, decoupling the singular points from the spatial discretization. To this purpose, we approximate the right-hand side of Eq. 4 with a discrete version of the Dirac delta distribution, with support on a small neighborhood of the well center.

We consider a classical approximation δ^{r_ε} (see also [93])

$$\delta_{w^{(\star)}}^{r_\varepsilon}(x, y) := \frac{\pi}{r_\varepsilon^2 (\pi^2 - 4)} \theta \left(\frac{d_{w^{(\star)}}(x, y)}{r_\varepsilon} \right), \tag{7}$$

where

$$d_{w^{(\star)}}(x, y) = \sqrt{(x - x_{w^{(\star)}})^2 + (y - y_{w^{(\star)}})^2}$$

denotes the distance from the center $(x_{w^{(\star)}}, y_{w^{(\star)}})$ of the well $w^{(\star)}$ and

$$\theta(r) := \begin{cases} \cos(\pi r) + 1, & \text{if } -1 < r < 1, \\ 0, & \text{otherwise.} \end{cases} \tag{8}$$

In Eq. 7, $r_\varepsilon > 0$ is an arbitrary (small, compared with the domain size, i.e., $r_\varepsilon \ll \text{diam}(\widehat{\boldsymbol{\Omega}})$) parameter that can be chosen depending on the well radius and on the suitable spatial discretization (near the well). For a visualization of δ^{r_ε} for different values of r_ε, see Fig. 6.

In practice, the singular term is defined in such a way that the physical solution, prescribed only outside the well, is continuously extended inside the well. As a consequence, the numerical solution will have a physical meaning only at a distance from the well center greater than or equal to r_ε.

One of the main advantages of the non-matching approach is that it allows to arbitrarily change the position of the well within the computational domain without the need of re-generating the computational mesh. This feature will be extremely important when solving the optimization problem related to the (arbitrary) optimal placement of the wells.
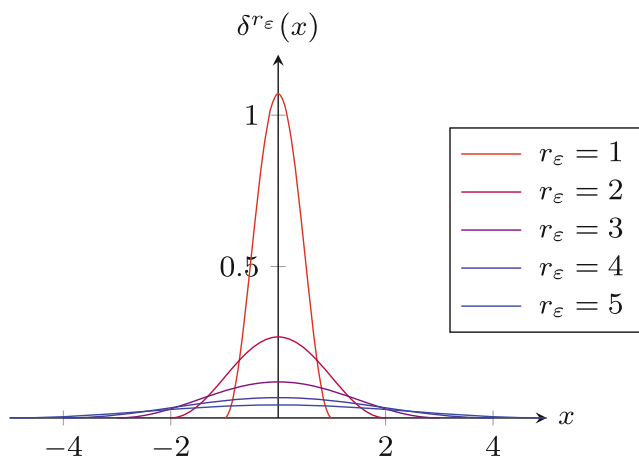
Fig. 6 Visualization of Eq. 7 for $y = y_{w(\star)}$ and $x_{w(\star)} = 0$. The function vanishes for the points at distance from $(x_{w(\star)}, y_{w(\star)})$ greater than r_ε. Notice that, for any $r_\varepsilon > 0$, the integral over $\bar{\Omega}$ of the function $\delta_{w(\star)}^{r_\varepsilon}$ is equal to one

3.3 Heat transport

This section describes in detail the modeling of heat transport, composed of an advection-diffusion equation for the temperature field and a reduced model for taking into account Dirichlet boundary conditions at the injection wells.

3.3.1 The advection-diffusion equation

The model for heat transport can be obtained from the standard energy conservation equation (see, e.g., [31]), resulting in a time-dependent advection-diffusion equation for a temperature field $T(t, \boldsymbol{x})$ (K):

$$\frac{\partial (\rho C T)}{\partial t} - \nabla \cdot (\lambda \nabla T) + \rho_f C_f \boldsymbol{u} \cdot \nabla T = 0 \tag{9a}$$
$$\text{in } (0, t^L] \times \boldsymbol{\Omega},$$

where it is assumed that heat creation through friction in the well and heat loss/gain from the outside can be neglected, yielding a right-hand side equal to zero. We complete Eq. 9a with the initial condition

$$T(0, \boldsymbol{x}) = T_0(\boldsymbol{x}) \quad \text{in } \boldsymbol{\Omega}, \tag{9b}$$

and the boundary conditions

$$T = T_{w_k^{\text{inj}}} \quad \text{on } \Gamma_{w_k^{\text{inj}}}, \ \forall k, \tag{9c}$$

$$T = T_0 \quad \text{on } \partial \boldsymbol{\Omega} \setminus \bigcup_k \Gamma_{w_k^{\text{inj}}}. \tag{9d}$$

Here, $k = 1, \ldots, N^{\text{inj}}$, N^{inj} is the number of injection wells, $T_{w_k^{\text{inj}}}$ (K) are the corresponding injection temperatures, and T_0 (K) refers to the initial temperature field, in this context called *formation or aquifer temperature*. Moreover, $\boldsymbol{u}$ (m/s) is the groundwater flow velocity, obtained from Eq. 1, t (s) is the time variable, and t^L (s) denotes the upper

bound on the time interval, coinciding with the maximum operational time of the geothermal installation in the considered problems.

In Eq. 9a, there are coefficients associated to the fluid (index f) and to the porous structure (index s), respectively, namely the densities ρ_f, ρ_s (kg/m^3) and the material-specific heat capacities C_f, C_s (J/kg K), which are combined to the volumetric (macroscopic) heat capacity, given by

$$\rho C := (1 - \phi) \rho_s C_s + \phi \rho_f C_f,$$

depending on the porosity ϕ.

The total thermal conductivity tensor λ (W/m K) can be modeled (see, e.g., [30, 96]) as the sum of the equivalent conductivity $\lambda_{eq} \mathbb{I}$ and thermal dispersion λ_{dis}, i.e., $\lambda = \lambda_{eq} \mathbb{I} + \lambda_{dis}$ with

$$\lambda_{eq} = (1 - \phi) \lambda_s + \phi \lambda_f,$$
$$\lambda_{dis} = \rho_f C_f \left(\alpha_T |\boldsymbol{u}| \mathbb{I} + (\alpha_L - \alpha_T) \frac{\boldsymbol{u} \boldsymbol{u}^T}{|\boldsymbol{u}|} \right). \tag{10}$$

In Eq. 10, λ_s and λ_f are the (scalar) thermal conductivities of the indexed species, α_L (m) is the longitudinal thermal dispersion, and α_T (m) denotes the transversal thermal dispersion.

As mentioned in (A4) and (A6), the transversal dispersion is neglected, assuming that its effect does not play a relevant role in the considered two-dimensional model and the assumption of temperature-independent densities and heat capacities further allows to exclude the respective terms from the temporal and spatial derivative.

3.3.2 Total simulation time

In our numerical simulations, the final simulation time t^L will be defined depending on two conditions. On the one hand, we consider a maximum admissible operational time of 80 years, which might depend on geological, engineering, and legal constraints. One the other hand, we consider also the so-called *specific lifetime* of the installation, which is defined as the time when the fluid temperature at a measurement point of a production well drops below a threshold temperature T_{quit} (K), i.e., it drops by more than 10% with respect to the aquifer temperature. The specific lifetime relates to the *economic lifetime* of a geothermal facility, commonly defined as a certain limit of production temperature under which it is no longer economic to proceed.

3.3.3 Reduced-order model for the injection well

As done for the flow model in Eq. 1, we consider a modified problem for the temperature field, defined on the

whole domain $\widehat{\boldsymbol{\Omega}}$, and in the limit case of the well radius tending to zero. To this purpose, we replace the Dirichlet boundary condition at the injection wells in Eq. 9c with appropriate terms, which allow to seek for a temperature field $T: (0, t^L] \times \widehat{\boldsymbol{\Omega}} \rightarrow \mathbb{R}$ that satisfies the condition Eq. 9c and obeys to Eq. 9a outside the wells. The considered temperature equation is based on a penalty method, i.e., we explicitly add terms that penalize deviations from the prescribed injection temperatures within the well regions. As a consequence, an explicit spatial discretization of the well boundary is no longer required, considerably reducing the complexity of the spatial discretization, especially in the framework of optimization.

Let us note that the temperature field is only disturbed at the injection wells such that solely these positions have to be included as heat sources. After dividing Eq. 9a by $\rho_f C_f$, we obtain

$$
a \frac{\partial T}{\partial t} - \nabla \cdot (d \nabla T) + \boldsymbol{u} \cdot \nabla T \\
+ \gamma \sum_{k=1}^{N^{\mathrm{inj}}} \frac{Q_{3D}^k}{H} \delta_{w_k} \left(T - T_{w_k} \right) = 0, \ \text{in} \ (0, t^L] \times \widehat{\boldsymbol{\Omega}}, \tag{11}
$$

with $a := \frac{\rho C}{\rho_f C_f}$, $d := \frac{\lambda}{\rho_f C_f}$, and a dimensionless penalty parameter $\gamma > 0$. Problem 11 is then completed with the boundary conditions

$$
\begin{aligned}
T(0, \boldsymbol{x}) &= T_0(\boldsymbol{x}) &&\text{in} \ \widehat{\boldsymbol{\Omega}}, \\
T &= T_0 &&\text{on} \ \partial \widehat{\boldsymbol{\Omega}}.
\end{aligned} \tag{12}
$$

3.4 Numerical method

The partial differential equations for groundwater flow and heat transport are solved using a finite element method (FEM). To this purpose, let us introduce a spatial discretization (a computational mesh) $\mathcal{T}_h$ of the extended domain $\widehat{\boldsymbol{\Omega}}$, composed of shape-regular triangular elements (non-degenerate, see [97, p. 124], [98, Def. 1.107]). The parameter $h > 0$ denotes the characteristic mesh size, which can be defined, e.g., as $h := \max_{\boldsymbol{T} \in \mathcal{T}_h} h_{\boldsymbol{T}}$, where $h_{\boldsymbol{T}}$ stands for the diameter of the mesh element $\boldsymbol{T} \in \mathcal{T}_h$. Further, we will abbreviate the standard L^2-product on $A \subset \widehat{\boldsymbol{\Omega}}$ by $(\cdot, \cdot)_A$.

3.4.1 Stationary Darcy–Brinkman equation

We employ a stabilized finite element method for the Brinkman problem, which has been recently described and analyzed in [99] and is designed to deal robustly with any choice of physical parameters (i.e., μ_{eff} and σ).

The numerical approximations of the velocity and the pressure are sought in the space of continuous, piecewise (on each triangle) linear polynomials

$$
\begin{aligned}
\boldsymbol{V}_h &:= \left\{ \boldsymbol{v}_h \in \boldsymbol{C}^0(\overline{\widehat{\boldsymbol{\Omega}}}) : \boldsymbol{v}_h|_{\boldsymbol{T}} \in \mathbb{P}_1(\boldsymbol{T}), \forall \boldsymbol{T} \in \mathcal{T}_h \right\}, \\
Q_h &:= \left\{ q_h \in L_0^2(\widehat{\boldsymbol{\Omega}}) \cap C^0(\overline{\widehat{\boldsymbol{\Omega}}}) : q_h|_{\boldsymbol{T}} \in \mathbb{P}_1(\boldsymbol{T}), \forall \boldsymbol{T} \in \mathcal{T}_h \right\}.
\end{aligned}
$$

The stabilized finite element formulation is obtained multiplying the momentum conservation equation by a function $\boldsymbol{v}_h \in \boldsymbol{V}_h$ and the mass conservation equation by $q_h \in Q_h$, and using integration by parts.

The choice of equal-order linear finite element spaces allows to reduce the computational complexity of the problem, especially when fine spatial discretizations are needed. In order to guarantee stability and convergence of the resulting numerical method, the inherent integral formulation needs to be modified, including so-called stabilization terms. We refer the interested reader to [99] (and references therein) for a detailed discussion on the stabilization methods.

The considered finite element problem reads then: Find $(\boldsymbol{u}_h, p_h) \in \boldsymbol{V}_h \times Q_h$ such that

$$
\begin{aligned}
\mu_{\mathrm{eff}} (\nabla \boldsymbol{u}_h, \nabla \boldsymbol{v}_h) &+ \sigma (\boldsymbol{u}_h, \boldsymbol{v}_h) - (p_h, \nabla \cdot \boldsymbol{v}_h) \\
+ (\nabla \cdot \boldsymbol{u}_h, q_h) &+ S_h [(\boldsymbol{u}_h, p_h), (\boldsymbol{v}_h, q_h)] \\
&= (g, q_h) + G_h [\boldsymbol{v}_h],
\end{aligned} \tag{13}
$$

for all $(\boldsymbol{v}_h, q_h) \in \boldsymbol{V}_h \times Q_h$. In Eq. 13, the source term g is defined as in Eq. 4 using Eq. 6 and the approximate delta function Eq. 7, and we have introduced the so-called non-symmetric GLS stabilization and the grad-div stabilization terms

$$
\begin{aligned}
S_h [(\boldsymbol{u}, p), (\boldsymbol{v}, q)] &:= \alpha \sum_{\boldsymbol{T} \in \mathcal{T}_h} \frac{h_{\boldsymbol{T}}^2}{\nu} (\sigma \boldsymbol{u} + \nabla p, \sigma \boldsymbol{v} + \nabla q)_{\boldsymbol{T}} \\
&\quad + \delta \nu (\nabla \cdot \boldsymbol{u}, \nabla \cdot \boldsymbol{v}), \\
G_h [\boldsymbol{v}] &:= \delta \nu (g, \nabla \cdot \boldsymbol{v}),
\end{aligned}
$$

where α and δ are positive stabilization parameters, and $\nu = \mu_{\mathrm{eff}} + \sigma \ell_{\boldsymbol{\Omega}}^2$, $\ell_{\boldsymbol{\Omega}}$ being a typical physical length scale of the problem, see [99].

Remark 2 (Stabilization parameters) The choice of the parameters α and δ might influence qualitatively the solution, but it does not affect its asymptotic order of convergence [99]. In the present work, we primarily selected the order of magnitude of these parameters following the recommendations of [99]. Moreover, we performed several preliminary tests in the validation settings (see Sections 3.6.1 and 3.6.3), in order to eventually select the value of the GLS stabilization parameter to be used in the remaining simulations.

3.4.2 Transient heat equation

In order to approximately solve the problem for the temperature field, Eq. 11, we utilize the regularized delta function Eq. 7 and define

$$
\begin{aligned}
c &:= \sum_{k=1}^{N^{\text{inj}}} \gamma \frac{Q_{w_{3D,k}^{inj}}}{H} \delta_{w_k^{inj}}^{r_\varepsilon}, \\
f &:= \sum_{k=1}^{N^{\text{inj}}} \gamma \frac{Q_{w_{3D,k}^{inj}}}{H} \delta_{w_k^{inj}}^{r_\varepsilon} T_{w_k^{\text{inj}}}.
\end{aligned} \tag{14}
$$

We discretize Eq. 11 in time via an implicit (backward) Euler scheme. Denoting with T^n the approximated temperature field at time t^n and with $\Delta t_n := t^n - t^{n-1}$ the time step, the time-discretized heat equation reads

$$
\begin{aligned}
aT^n &+ \Delta t_n \left(-d\Delta T^n + \boldsymbol{u} \cdot \nabla T^n + cT^n \right) \\
&= aT^{n-1} + \Delta t_n f^n \quad \text{in } \widehat{\boldsymbol{\Omega}}.
\end{aligned} \tag{15}
$$

As next, we discretize Eq. 15 in space using a finite element method, seeking the solution in the space of continuous and piecewise linear functions:

$$
\mathbb{T}_h := \left\{ s_h \in C^0(\overline{\widehat{\boldsymbol{\Omega}}}) \colon s_h|_{\boldsymbol{T}} \in \mathbb{P}_1(\boldsymbol{T}), \forall \boldsymbol{T} \in \mathcal{T}_h \right\}.
$$

The finite element formulation reads: Find $T_h^n \in \mathbb{T}_h$ with $T_h^n|_{\partial\widehat{\boldsymbol{\Omega}}} = T_0$ such that

$$
\begin{aligned}
a\left(T_h^n, s_h\right) &+ \Delta t_n \left(d\nabla T_h^n, \nabla s_h\right) \\
&+ \Delta t_n \left(\boldsymbol{u} \cdot \nabla T_h^n + cT_h^n, s_h\right) \\
&= a\left(T_h^{n-1}, s_h\right) + \Delta t_n \left(f^n, s_h\right), \\
&\qquad \forall s_h \text{ in } \mathbb{T}_h \text{ with } s_h|_{\partial\widehat{\boldsymbol{\Omega}}} = 0.
\end{aligned} \tag{16}
$$

Remark 3 (On the penalty parameter γ) The penalty parameter γ in Eq. 14 influences the time required to enforce a temperature equal to the injection temperature within the circular region of radius r_ε.

3.5 Optimization of energy production

Based on the above described computational model, the goal of this work is to propose an efficient algorithm for computing the parameters describing deep geothermal installations (e.g., well locations) that maximize the net energy production—also called doublet/triplet/etc. capacity—subject to geological, ecological, and economic restrictions.

3.5.1 Problem setting

Let us assign to each well a pump efficiency $\varepsilon_{w^{(\star)}} \in (0, 1]$ and a recharge or discharge rate $Q_{w^{(\star)}}$ (m^3/s). The net

energy E_{net} (J) produced in the maximum operational time t^L (s) is given by

$$
E_{\text{net}} := \int_0^{t^L} \left(e_{\text{prod}}(t) - e_{\text{pump}}(t) \right) dt, \tag{17}
$$

where

$$
e_{\text{prod}}(t) = \rho_f C_f \left(\sum_{l=1}^{N^{\text{prod}}} Q_{3D,w_l} T_l(t) - \sum_{k=1}^{N^{\text{inj}}} Q_{3D,w_k} T_k(t) \right)
$$

stands for the energy flux gained through the heat transfer, while

$$
e_{\text{pump}}(t) = \sum_{j=1}^{N^{\text{prod}}+N^{\text{inj}}} \frac{Q_{3D,w_j}}{\varepsilon_{w_j}} \left| \Delta p_{w_j}(t) \right|
$$

denotes the energy flux that has to be invested in the operation of the pumps and represents energy losses. In e_{prod}, T_l and T_k stand for the temperatures at the wells l and k, while Δp_{w_j} denotes the pressure difference with respect to the ambience/reference pressure induced by the pump at the respective well.

Assuming that the lifetime interval $[0, t^L]$ is subdivided into N_t sub-intervals of equal length Δt, we approximate the net energy as

$$
E_{\text{net}} = \sum_{i=1}^{N_t} \Delta t \left(e_{\text{prod}}(i\Delta t) - e_{\text{pump}}(i\Delta t) \right). \tag{18}
$$

The optimization problem consists then in finding the positioning of wells that maximizes the energy production E_{net}. Notice that E_{net} depends on the well locations $\left\{ (x_{w^{(\star)}}, y_{w^{(\star)}}) \right\}$ through the pressure and the temperature fields, as well as through the total operation time t^L (see Section 3.3.2).

The considered optimization problem for the multiple well placement aims at minimizing the pressure difference between injection and production wells while maximizing the time until the *thermal breakthrough*—the time at which the temperature at a production well drops below the formation temperature—takes place. After the occurrence of the thermal breakthrough, the temperature decline speed at the production wells is decisive for the resulting net energy.

Remark 4 (Constraint on the inter-well distance)
From the reservoir engineering viewpoint, a reasonable and economic prerequisite for any deep geothermal installation is that the injection and production rates are chosen according to the given permeability structure of the targeted reservoir region such that energy can be extracted as long as possible, within the estimated scheduled operational time.

It is worthwhile noting that the distance, and thus the geometric parameters, between injection and production

wells can only be varied within a reasonable range since sufficient hydraulic connectivity between injection and production wells should be practically guaranteed. Hence, when it comes to the optimization of the geothermal energy production by multiple wells, not only the optimal placement of the wells in the reservoir is searched for but also the optimal distance relative to each other plays an important role for the different multiple well arrangements.

Remark 5 (Model limitations)

As described earlier, the employed non-matching immersed boundary method (Sections 3.2.2 and 3.3.3) incorporates the wells in the modeling domain. It provides a physically meaningful solution only starting from a distance r_ε (larger than the well radius) from the center of the well. Hence, pressure and fluid temperature cannot be exactly evaluated at the well boundary, yielding in practice slightly more pessimistic estimates for the net energy and the economic lifetime. On the other hand, it is reasonable to assume that this approximation does not have a significant influence on the simulation results for optimal placement. Related to the model dimension reduction, injection and production pressures used in the energy computation are evaluated at the level of the aquifer (i.e., *bottomhole pressure* (BHP), *bottomhole temperature* (BHT)). These pressures differ from the pump pressures at the ground level of the geothermal plant. Therefore, when computing the energy, we neglect the work needed to pump water from the surface to the bottomhole of the injection well and from the bottomhole of the production well up to the plant.

3.5.2 Optimization algorithm

The energy optimization problem is solved iteratively using a *gradient-free* (or derivative-free) method, i.e., searching the extrema of the cost functional only using function values. These algorithms do not require the computation of the gradient of the cost functional, which typically leads to the solution of additional problems and further necessary steps, i.e., an increased computational time, especially for coupled and time-dependent problems. Additionally, they might converge towards suboptimal solutions (such as local minima), thus reducing the accuracy of the solution.

Each iteration of the optimization algorithm requires one or more evaluations of the functional to be maximized (e.g., Eq. 18). A functional evaluation consists of the following steps (Fig. 7, top): for a given well configuration (the control variables), we compute the corresponding (steady) flow solution, then solve the temperature equation up to the maximum operation time, or until the thermal breakthrough happens, computing then the total net energy.

At each optimization step, the search algorithm performs a sampling of the parameter space, evaluating different con-
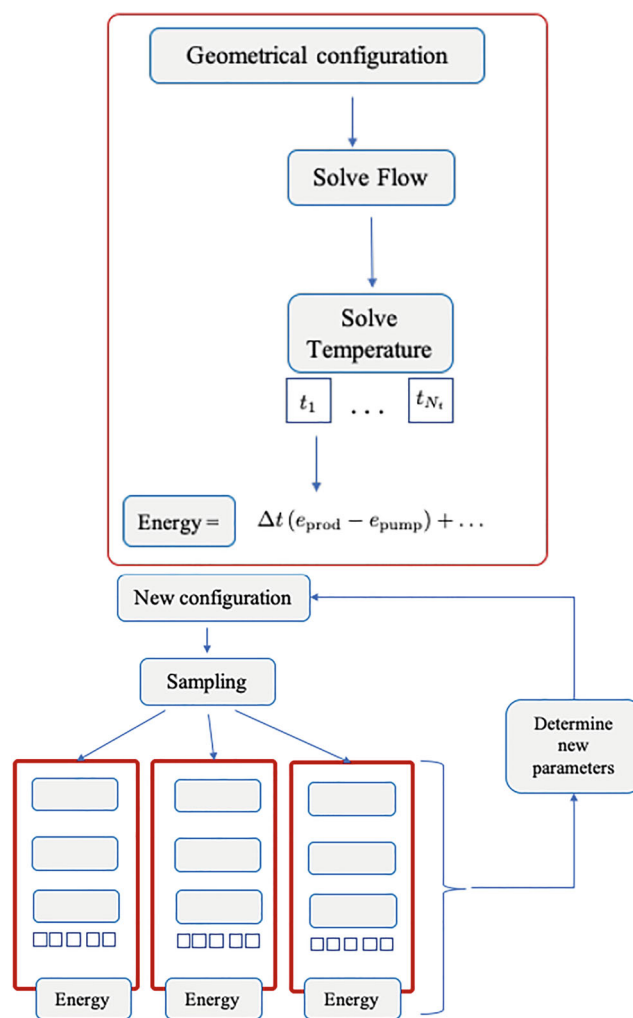

Fig. 7 Top: The different steps for the computation of the net energy for a given geometrical configuration. Bottom: Sketch of the iterative optimization procedure. Each box contains the steps specified in the top figure for the evaluation of net energy

figurations close to the current state (Fig. 7, bottom), then selecting a new configuration based on different criteria depending on the particular method. In order to reduce the bias of local minima, we performed the same amount of optimization steps in all cases, defining the optimal solution as the configuration with the overall higher net energy.

In our numerical investigation, we considered global and local optimization algorithms. The former class (global methods) explores at each iteration the whole parameter space, while the latter (local methods) focus on the parameter space in the vicinity of the current value. Our preliminary study revealed that the local variants might converge faster but at the same time they might be trapped in a local minimum, i.e., not yielding a similarly optimal (with respect to the functional value) result at the global level.

Therefore, in the numerical results (presented in Section 5), we show the outcome of the global optimization algorithm DIRECT-L [100]. This is a deterministic approach, based on decomposing the search domain into hyperrectangles and using successive refinement.

3.6 Validation and benchmarking of the numerical solver

The finite element library ParMooN has been used and validated in several publications [45, 101], including fluid flow in porous media [99]. The scope of this section is to assess the finite element solver and the accuracy of the immersed boundary method considering a setting particularly relevant for the problem of interest.

3.6.1 Fluid flow

We start with a simple one-well problem, considering the annular domain

$$\Omega := \left\{ (x, y) \in \mathbb{R}^2 \ : \ r_0^2 \leqslant x^2 + y^2 \leqslant r_1^2 \right\} \tag{19}$$

with $r_0 := 0.2\,\mathrm{m}$ and $r_1 := 1000\,\mathrm{m}$, perforated by an injection well

$$w^{\mathrm{inj}} := \left\{ (x, y) \in \mathbb{R}^2 \ : \ x^2 + y^2 \leqslant r_0^2 \right\}$$

with boundary $\Gamma_{w^{\mathrm{inj}}} := \partial w^{\mathrm{inj}}$ (a circle of radius r_0).

For the immersed boundary approach, we introduce the extended domain

$$\Omega \cup w^{\mathrm{inj}} = \left\{ (x, y) \in \mathbb{R}^2 \ : \ x^2 + y^2 \leqslant r_1^2 \right\}$$

and use the discrete Dirac delta function Eq. 7 with $r_\varepsilon = 50\,\mathrm{m}$. Hence, the numerical solution is expected to behave as the physical one at a distance from the origin larger than 50 m.

In order to assess the capability of the finite element solver in approximating the solution near the wells, we consider porous media flow described by the Darcy equations (groundwater flow equations), i.e., $\mu_{\mathrm{eff}} = 0$, with non-homogeneous Dirichlet boundary conditions for the velocity imposed on $\Gamma_{w^{\mathrm{inj}}}$ and homogeneous pressure boundary conditions on the outer boundary, i.e.,

$$\begin{aligned} \boldsymbol{u} \cdot \boldsymbol{n} &= U_{w^{\mathrm{inj}}} && \text{on } \Gamma_{w^{\mathrm{inj}}}, \\ p &= 0 && \text{on } \partial \Omega \setminus \Gamma_{w^{\mathrm{inj}}}, \end{aligned} \tag{20}$$

for some $U_{w^{\mathrm{inj}}} \in \mathbb{R}$ and vanishing source terms. In this setting, the system Eq. 1a–Eq. 1b admits the analytic solution

$$\begin{aligned} \boldsymbol{u}^{sol}(x, y) &= \frac{U_{w^{\mathrm{inj}}} r_0}{x^2 + y^2} \begin{pmatrix} x \\ y \end{pmatrix}, \\ p^{sol}(x, y) &= \sigma U_{w^{\mathrm{inj}}} r_0 \log \left(\frac{r_1}{\sqrt{x^2 + y^2}} \right) \end{aligned} \tag{21}$$
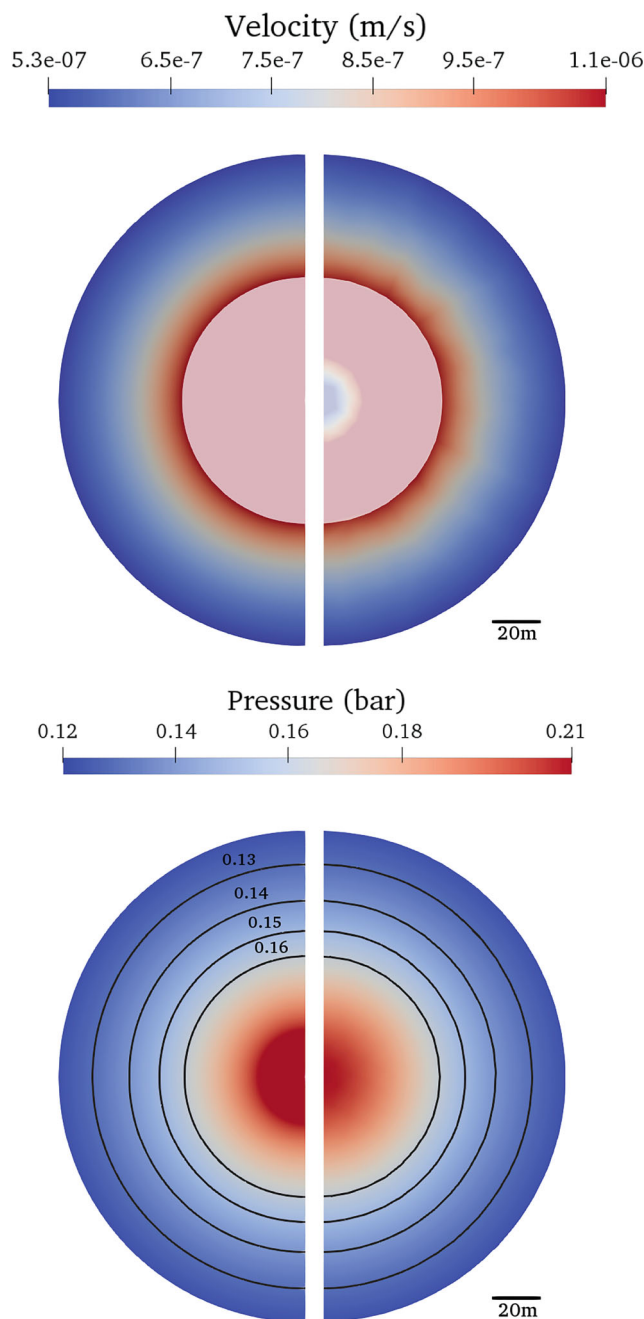

Fig. 8 Velocity field (top) and pressure field with selected contours (bottom) in a centered cutout of radius 100 m, resulting from a single injection well operated with a constant flow rate of 100 l/s. The artificial well has a higher transparency than the rest of the modeling domain (top). The exact solution $\boldsymbol{u}^{sol}$ respectively p^{sol} is shown in the left halves, while the velocity and pressure fields, obtained with the immersed method, are depicted in the right halves

(notice that the velocity and the pressure fields are well defined only in the physical domain Ω). For the numerical tests, we take $\mu = 0.0003\,\mathrm{kg/m\,s}$, $K = 3 \cdot 10^{-12}\,\mathrm{m}^2$, yielding $\sigma = 10^8\,\mathrm{kg/m^3\,s}$, and $\ell_\Omega = 50\,\mathrm{m}$. Moreover, we use $Q_{3D,w^{\mathrm{inj}}} = 100\,\mathrm{l/s}$, calculate $U_{w^{\mathrm{inj}}} = \frac{Q_{3D,w^{\mathrm{inj}}}}{2\pi r_0 H}$
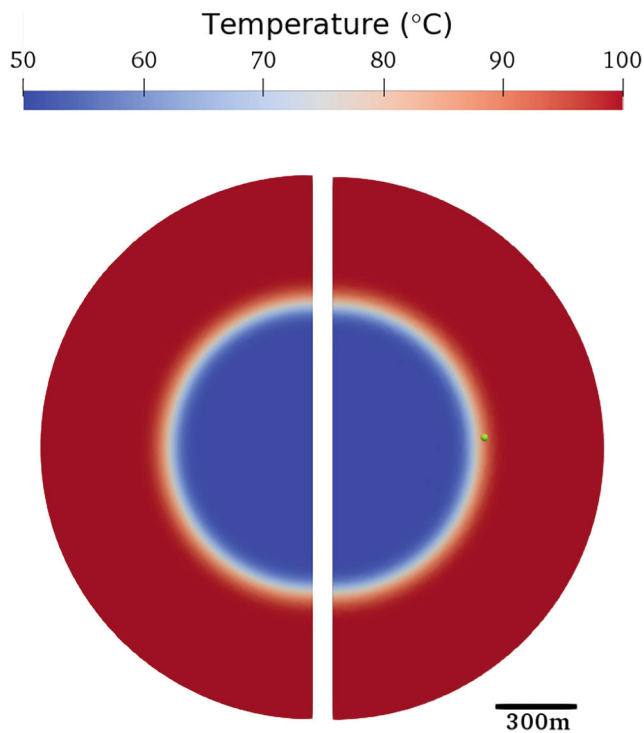
Fig. 9 Temperature distribution at simulation time $t = 50$ years in the annular domain resulting from a single injection well operating with 1001/s constant flow rate. The left half is the solution obtained prescribing the Dirichlet boundary condition ($T = 50°C$) on the well boundary, while the right half of the plot shows the solution using the immersed boundary approach. The green point has the coordinates $(560, 40)$ m

Fig. 10 Evolution of temperature at the point $(x, y) = (560, 40)$ m in the simulation of an annular domain and a single injection well operating with 1001/s constant flow rate. We compare the solution obtained imposing the Dirichlet boundary condition (blue crosses) with the immersed boundary one (orange line)

as described in Eq. 2, and use the remaining parameters as given in Table 6. We use a triangular mesh with about 17,500 vertices and 35,000 triangles, whose diameter is between $h_{\min} = 6.85$ m and $h_{\max} = 27.90$ m.

In Fig. 8, we compare the exact solution $\left(\boldsymbol{u}^{sol}, p^{sol} \right)$, which is defined only outside the well with radius r_0, i.e. in $\boldsymbol{\Omega}$, with the numerical solution obtained via the immersed boundary method with $r_\varepsilon = 50$ m, i.e., solving Eq. 13 on $\widehat{\boldsymbol{\Omega}}$. We visualize onehalf of a circular, centered cutout of radius 100 m from the respective domain ($\boldsymbol{\Omega}$ and $\widehat{\boldsymbol{\Omega}}$).

The tests confirm that the resulting velocity and pressure fields approximate well the exact solution for radii larger than or equal to r_ε. In particular, the pressure isolines (for the immersed method) fit well with those for the exact solution.

3.6.2 Heat transport

As next step, we assess the effect of the penalty-based method, employed to impose the Dirichlet boundary condition on the boundary of the wells for the heat transport problem, Eq. 11, on the resulting temperature field. To that
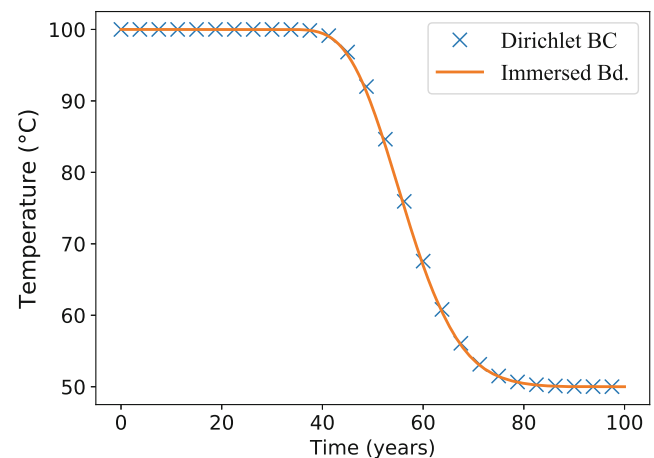
end, we consider the single well domain $\boldsymbol{\Omega}$ defined in Eq. 19 and the advective field $\boldsymbol{u}^{sol}$ defined in Eq. 21.

The temperature is prescribed at the inner circle, while at the outer circle we impose a homogeneous Neumann boundary condition. All remaining parameters in Eq. 9 and Eq. 11 are chosen as described in Table 6.

We compare (i) the temperature field obtained imposing strongly the Dirichlet boundary condition at the well boundary as in Eq. 9 with (ii) the temperature field computed via the penalty-based immersed boundary method Eq. 16.

In the following computations, we use for $\boldsymbol{\Omega}$ a mesh with 20 nodes on $\Gamma_{w^{\text{inj}}}$ and 160 nodes on the outer circular boundary, resulting in 24,022 triangles, $h_{\min} = 0.064$ m, $h_{\max} = 55.40$ m, and 12,100 mesh nodes. For $\widehat{\boldsymbol{\Omega}}$, a mesh with 20 nodes uniformly distributed along the artificial well boundary with radius $r_\varepsilon = 50$ m is considered instead, resulting in a coarser grid with 8657 triangles, $h_{\min} = 13.75$ m, $h_{\max} = 55.49$ m, and 4409 mesh nodes.

The results displayed in Figs. 9 and 10 compare the temperature fields after 50 years (Fig. 9) and the temperature evolution at a specified point (Fig. 10). They show good agreement between the solutions of approaches (i) and (ii). It shall be mentioned that the progressing cooling front (Figs. 9 and 10) computed with the penalty method is slightly faster than the one obtained with the classically imposed Dirichlet boundary condition (the difference is about 0.5 years). This effect is due to the fact that in the penalty approach, the inner temperature is immediately imposed at the radius r_ε, which is larger than the actual physical well, whereas in the case of the strongly imposed Dirichlet boundary condition, the cold water thermal front reaches r_ε only after few iterations.

Table 1 Specific lifetimes in years for varying domain size (in km^2) and time step length (in years)

$\mid\widehat{\boldsymbol{\Omega}}\mid$ (km^2) (DOFS)	3×3 (43,657)	5×5 (44,203)	8×8 (46,042)	10×10 (47,549)	15×15 (52,536)
$\Delta t = 1\,\text{year}$	55 $\overset{-5.46\%}{\longrightarrow}$ $\downarrow\,+2.73\%$	52 $\overset{-1.92\%}{\longrightarrow}$ $\downarrow\,+2.89\%$	51 $\overset{0\%}{\longrightarrow}$ $\downarrow\,+2.94\%$	51 $\overset{0\%}{\longrightarrow}$ $\downarrow\,2.94\%$	*51* $\downarrow\,+1.96\%$
$\Delta t = \tfrac{1}{2}\,\text{years}$	56.5 $\overset{-5.31\%}{\longrightarrow}$ $\downarrow\,+1.77\%$	53.5 $\overset{-1.87\%}{\longrightarrow}$ $\downarrow\,+1.40\%$	52.5 $\overset{0\%}{\longrightarrow}$ $\downarrow\,+1.91\%$	52.5 $\overset{-0.95\%}{\longrightarrow}$ $\downarrow\,+0.95\%$	*52* $\downarrow\,+1.44\%$
$\Delta t = \tfrac{1}{4}\,\text{years}$	57.5 $\overset{-5.65\%}{\longrightarrow}$ $\downarrow\,+0.57\%$	*54.25* $\overset{-1.38\%}{\longrightarrow}$ $\downarrow\,+0.61\%$	53.5 $\overset{-0.94\%}{\longrightarrow}$ $\downarrow\,+0.62\%$	*53* $\overset{-0.47\%}{\longrightarrow}$ $\downarrow\,+1.09\%$	*52.75* $\downarrow\,+0.95\%$
$\Delta t = \tfrac{1}{12}\,\text{years}$	57.83 $\overset{-5.62\%}{\longrightarrow}$	*54.58* $\overset{-1.37\%}{\longrightarrow}$	53.83 $\overset{-0.46\%}{\longrightarrow}$	53.58 $\overset{-0.62\%}{\longrightarrow}$	*53.25*

The italic values indicate a total variation less than 2% with respect to the subsequent temporal refinement and domain size increase. All quantities are rounded to two decimal places

On the other hand, since this artifact is present in all considered geometrical configurations, we assume that it only marginally affects the result of the forthcoming comparative optimization studies—provided that r_ε is sufficiently small.

3.6.3 Single doublet: mesh- and boundary condition-independence studies

The purpose of this last validation step is to perform an extensive preliminary study concerning the influence of the spatial and temporal discretization, as well as the boundary conditions. The model setup consists of a single doublet, i.e., one production and one injection well with fixed inter-well distance of 1000 m and flow rates $Q_{w^{\text{prod}}} = Q_{w^{\text{inj}}} = 100\,\text{l/s}$. All remaining physical parameters are defined as in Table 6.

The wells are placed horizontally and vertically centered in a computational domain $\widehat{\boldsymbol{\Omega}}$ of varying size, which is discretized with a non-uniform triangular mesh. A subregion of size $2.4 \times 1.4\,\text{km}^2$ contains the doublet, is discretized with computational meshes of increasing resolution, and embedded in a coarser mesh. We monitor the specific lifetime of the doublet (see Section 3.3.2), varying the size of the smallest triangles, the time step size, and the size of the domain (i.e., the distance between the wells and

Table 2 Specific lifetimes in years (time step equals 3 months) for refinements of the subdomain 2.4×1.4 km^2 (characterized by $h_{\min}$) in the 10×10 km^2 modeling domain

Mesh size ($h_{\min}, h_{\max}$) (m)	Specific lifetime (years)
(51.0751, 259.815)	57.75 $\downarrow\,-8.66\%$
(28.2705, 267.206)	52.75 $\downarrow\,+0.47\%$
(12.8648, 267.206)	*53* $\downarrow\,0\%$
(6.14902, 262.21)	*53* $\downarrow\,+0.94\%$
(2.93729, 262.183)	*53.5*

The italic values visualize less than 1% variation with respect to the subsequent refinement

the outer boundary of the modeling domain). The threshold temperature at the production well is defined as $T_{\text{quit}} = 90°\text{C}$.

Table 1 summarizes the results of the investigation concerning the time step length and the distance to the outer boundary of the modeling domain. In particular, it can be seen that the boundary has a negligible effect on the specific lifetime of the doublet whenever it has a distance of about $\geqslant 3.5$ km from the wells which corresponds here to a domain size 8×8 km^2 or larger. Concerning the time discretization, results become almost independent (variation of less than $\approx 1\%$) of the chosen time step for values below 3 months.

The results compiled in Table 2 show that the mesh width in the active region has an impact on the specific lifetime. Too coarse meshes (row 1) seem to yield a significantly overestimated specific lifetime but differences for the smaller mesh sizes are relatively small. A mesh size of less than 28 m already assures a variation slightly below 1%. Note that the mesh size should be chosen in dependence of the artificial well diameter, which is $2r_\varepsilon$.

Finally, we use the information gained in the previous studies to set up and simulate an appropriate doublet configuration. Figures 11, 12, and 13 show the simulation results concerning velocity, pressure, and temperature fields at the end of the specific lifetime in the active subregion of size 2.4×1.4 km^2 with mesh size $h = 6.15$ m ($h = 262.21$ m elsewhere in the modeling domain), time step $\Delta t = 3$ months, and modeling domain size 10×10 km^2. The distance between injection well (left) and production well (right) is equal to 1000 m, the permeability is constant with value $K = 3 \cdot 10^{-12}$ m^2, and thermal dispersion has been omitted. All parameters that were not defined in this subsection are set as described in Table 6.
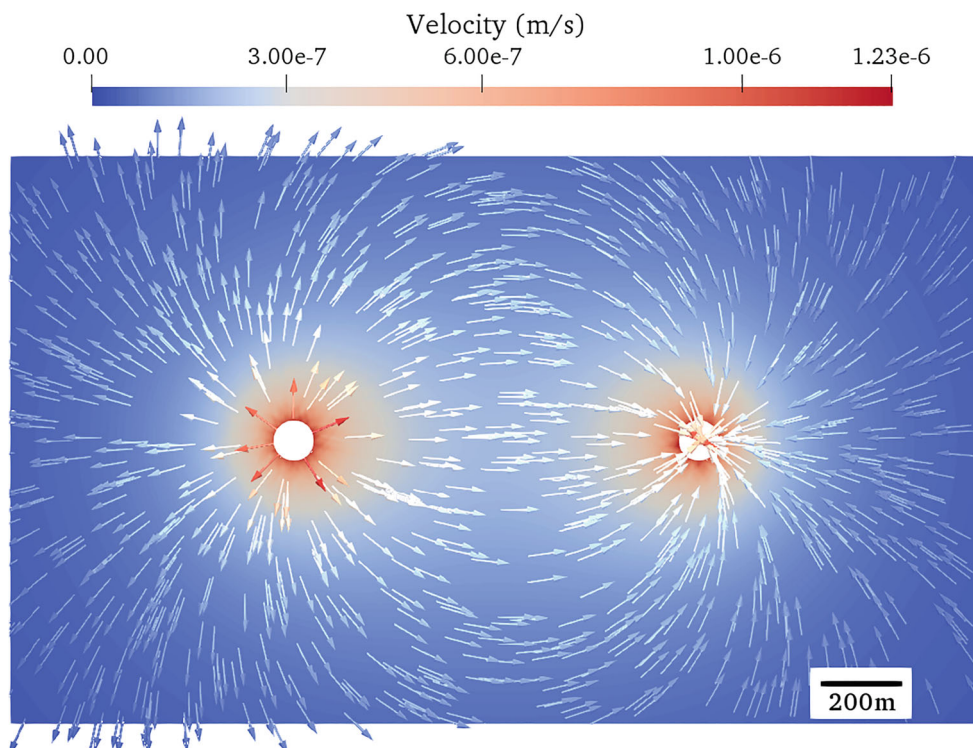
The arrows in the visualization of the velocity (Fig. 11) indicate that the flow is directed from the injection well (left) towards the production well (right). Due to the homogeneity of the domain and the same flow rates at both wells, the pressure (Fig. 12, top) is symmetric with respect to the isoline 0 bar (except for the sign). The pressure build-up and draw-down (also called *groundwater impression and*

Fig. 11 Magnitude of the velocity with unscaled arrows for the doublet setup with injection and production rate equal to 100 l/s

depression cones) are shown in Fig. 12 (bottom) and reveal a steep gradient in the vicinity of the wells only.

The cold water plume after 53 years of constant doublet operational scheme is surrounded by the contour line (green) referring to the minimum operation temperature of 90°C and has the typical tear drop shape towards the production well, see Fig. 13.

4 Model setups

The different configurations analyzed in this work are inspired by previous geothermal multi-well arrangements considered in different geothermal projects worldwide for several purposes (see, e.g., [18, 102]). From the reservoir management viewpoint, another important motivation behind our study constitutes the strikingly dynamic geothermal development for district heating in the Greater Munich region and related urgent questions. To this purpose, various geothermal reservoir settings similar to the ones encountered in the Upper Jurassic carbonates in the Greater Munich region are implemented and simulated within the proposed optimization framework. In particular, we focus on geothermal multiple doublet arrays (*lattice*) and smart multi-well *hexagonal* configurations.

An arrangement similar to the hexagonal multi-well configuration is currently being implemented around a major fault damage zone at the geothermal site Heiz-

kraftwerk Süd in the Schäftlarnstraße (Munich) in the form of multi-lateral wells, which are drilled from one common surface location. Future multi-well arrangements are planned in the city of Munich. Hence, the considered configurations may serve as a starting point for further analyses on smart geothermal multi-well arrangements in mega cities, where the heat demand is substantial and an evident lack of space problem is existing [14, 15, 103].

In both cases, we investigate different simulation scenarios characterized by:

– Heterogeneous geological conditions,
– Boundary and initial conditions (temperature),
– Production and injection wells (and flow rates).

4.1 Lattice

The lattice configuration is composed of doublet arrays, consisting of 8 injection and 8 production wells, arranged in form of a 4 rows × 4 columns lattice. In each row, two doublets are placed, where injection and production sites appear staggered: rows 1 and 3 start with a production well, whereas rows 2 and 4 start with an injection well (see Fig. 14, left). The same constant flow rates of 100 l/s are imposed for all wells, i.e., in total 1600 l/s.

Different scenarios are generated varying the permeability structure, the temperature initial and boundary conditions, and the control variables of the optimization procedure.

Fig. 12 Simulation results concerning a doublet setup with injection and production rate equal to 100 1/s. Top panel: Pressure with isolines. Bottom panel: Pressure along the direct line connecting the injection and production well
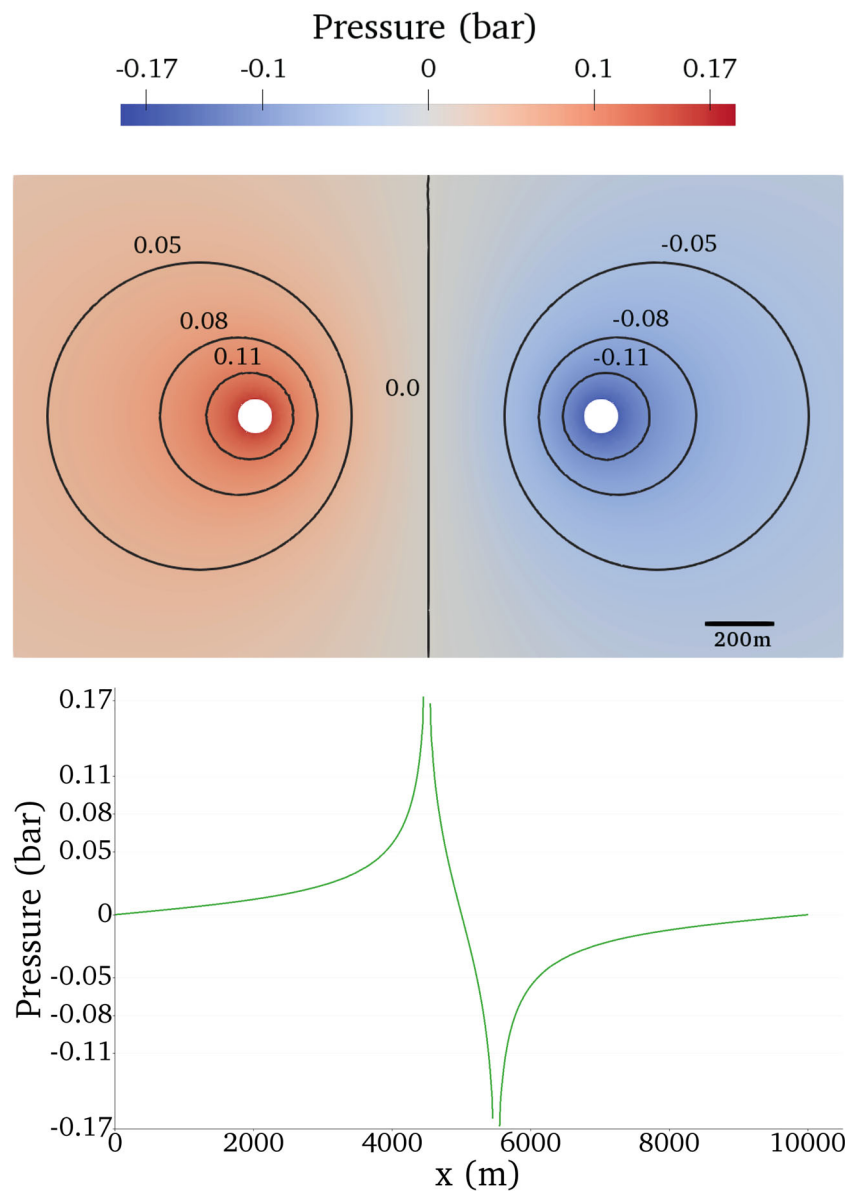
Permeability structure. Firstly, we consider a horizontally varying permeability structure with two different permeabilities:

$$K = \begin{cases} 3 \cdot 10^{-15}\,\mathrm{m}^2, & \text{for } 5.5\,\mathrm{km} \le x \le 7\,\mathrm{km}, \\ 3 \cdot 10^{-15}\,\mathrm{m}^2, & \text{for } 8.5\,\mathrm{km} \le x \le 9\,\mathrm{km}, \\ 3 \cdot 10^{-12}\,\mathrm{m}^2, & \text{elsewhere}, \end{cases} \quad (22)$$

This is intended to resemble two different carbonate facies such as bedded and reef facies as typically encountered in the Upper Jurassic carbonates in the Munich region as indicated in Fig. 14, left.

Aquifer temperature. Secondly, we distinguish between (i) constant initial and boundary temperature conditions and (ii) a dipping aquifer with linearly varying initial and boundary temperature conditions.

In order to asses the impact of geometrical parameters of the lattice arrangement on the net energy, different scenarios with varying control variables in particular for heterogeneous temperature and permeability fields are examined. For each case, we seek the optimal position of the wells with respect to the produced net energy (Eq. 18).

Multi-well configurations. The degrees of freedom for the search of optimized configurations (here concerning the movement of the wells) are referred to as the control variables. In a first scenario, we fix the position of the lattice center at the center of the domain and consider variations of the *lattice size* (i.e., the distance between closest wells) and rigid rotations. Thereby, the lattice size is allowed to vary between 500 and 1414 m, while the *rotation angle* cannot exceed 180° due to symmetry. In a second scenario, we

Fig. 13 Simulation results concerning a doublet setup with injection and production rate equal to 100 l/s and injection temperature 50°C.: Temperature distribution after 53 years of operation with an isoline (green) highlighting 90°C isotherm
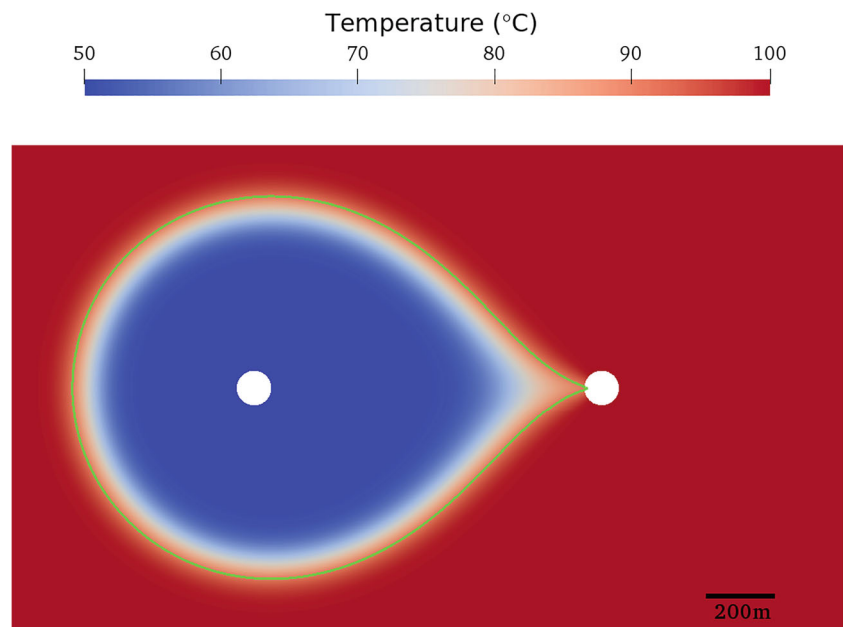
Fig. 14 Sketch of the $6 \times 6\,\text{km}^2$ (centered) subdomain for the lattice (LC, left) and hexagon ($H_{(2,4)}$, right) configurations. The dashed line confining the fault damage zone for the hexagon is variable in its distance with respect to the solid line. ⊕ indicates injection wells, ⊖ indicates production wells, and patterned and plain regions indicate two different permeabilities
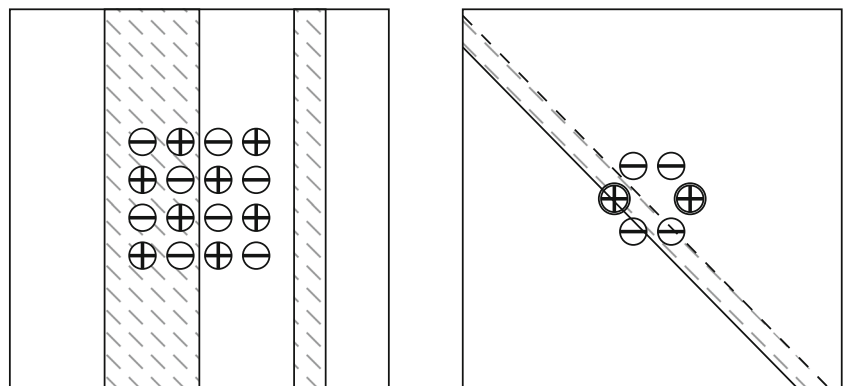
Table 3 Permeability structures, initial temperature distributions, and control variables for the optimization in the considered lattice scenarios (doublet arrays). Lattice size refers to the variation of the lattice dimensions, whereas position (x) and rotation angle refer to the translation forwards and backwards along the x-axis and rotation with respect to the lattice center, respectively

Scenario	Permeability	Initial temp.	Control variables
LC	Heterogeneous, Eq. 22	Constant, Eq. 25	Lattice size, rotation angle
L1	Heterogeneous,Eq. 22	Linear, Eq. 26	Lattice size, rotation angle
L2	Homogeneous ($K = 3 \cdot 10^{-12}\,\text{m}^2$)	Linear, Eq. 26	x-translation, rotation angle
L3	Heterogeneous, Eq. 22	Linear, Eq. 26	x-translation, rotation angle

Table 4 Permeability structures (including damage zone widths), well types along the hexagon (counter-clockwise, starting from the positive x-axis), and corresponding total flow rates for the considered hexagonal multi-well configurations

Scenario	Permeability	Width^{dz}	Wells	Total flow rate
$H_{(3,3)}$	Eq. 24	400 m	$\oplus \ominus \oplus \ominus \oplus \ominus$	600 l/s
$H_{(4,2)}$	Eq. 24	400 m	$\oplus \oplus \ominus \oplus \oplus \ominus$	400 l/s
$H_{(2,4)}1$	Eq. 24	400 m	$\oplus \ominus \ominus \oplus \ominus \ominus$	400 l/s
$H_{(2,4)}2$	Eq. 24	400 m (centered)	$\oplus \ominus \ominus \oplus \ominus \ominus$	400 l/s
$H_{(2,4)}3$	Eq. 23	200 m (healed)	$\oplus \ominus \ominus \oplus \ominus \ominus$	400 l/s

$\oplus$ indicates injection wells, while $\ominus$ stands for production wells

fix the lattice size equal to 600 m, allowing a rigid rotation in $(0°, 180°)$ and a rigid horizontal displacement with a maximal absolute value of 1221 m with respect to the initial position. The considered setups are summarized in Table 3.

4.2 Hexagon

In this case, we consider an equilateral hexagonal multi-well structure embedded in heterogeneous modeling domains.

The heterogeneities in the reservoirs are characterized as fault damage zones, delimited by two lines (see Fig. 14, right). We seek for the optimal configuration varying the radius of the hexagon between 500 and 2800 m and rigidly rotating the hexagon up to 180° with respect to its center, which is also the center of the modeling domain.

The different scenarios are described below and summarized in Table 4.

Permeability structure. We consider two cases, depending on whether the center of the hexagon is located within the fault damage zone or outside of it. In the first case (hexagon center within the damage zone), we consider a damage zone with a width of 400 m, which is formally defined by the lines passing through the two domain points: $(a_1, 0)$ and $(0, a_1)$ (lower line in Fig. 14, right) and $(a_2, 0)$ and $(0, a_2)$ (upper line in Fig. 14, right). We use $a_1 = 13,717.66$ m and $a_2 = 14,282.3$ m.

In the second setup (hexagon center outside the damage zone), we consider fault damage zones of different widths, i.e.,

$$\text{width}^{dz} \in \{100, 200, 300, 400\} \text{ m}.$$

The setups are obtained considering the lines passing through the points $(a_3, 0)$ and $(0, a_3)$, and $(a_3 + \sqrt{2}\,\text{width}^{dz}, 0)$ and $(0, a_3 + \sqrt{2}\,\text{width}^{dz})$, with $a_3 = 13,400$ m.

We further distinguish two different permeability structures: (I) with a weakly healed fault damage zone:

$$K = \begin{cases} 3 \cdot 10^{-12}\,\text{m}^2, & \text{fault damage zone,} \\ 3 \cdot 10^{-11}\,\text{m}^2, & \text{elsewhere,} \end{cases} \quad (23)$$

and (II) with a hydraulically active fault damage zone (i.e., a *leak fault*):

$$K = \begin{cases} 3 \cdot 10^{-12}\,\text{m}^2, & \text{fault damage zone,} \\ 3 \cdot 10^{-15}\,\text{m}^2, & \text{elsewhere.} \end{cases} \quad (24)$$

Multi-well configurations. In addition, the following scenarios are considered:

$H_{(3,3)}$: 3 injection and 3 production wells (alternated) along the hexagon and the flow rates 100 l/s (for all wells),

$H_{(4,2)}$: 4 injection and 2 production wells, injection rates $Q_{w^{\text{inj}}} = 50$ l/s, production rates $Q_{w^{\text{prod}}} = 100$ l/s,

$H_{(2,4)}$: 2 injection and 4 production wells, injection rates $Q_{w^{\text{inj}}} = 100$ l/s, production rates $Q_{w^{\text{prod}}} = 50$ l/s.

The last setup is additionally considered on the one hand with a permeable damage zone of diameter 400 m containing the center of the hexagon (permeability defined in Eq. 24) and on the other hand with a slightly healed damage zone (permeability defined in Eq. 23) of diameter 200 m.

4.3 Computational domain

The conceptual 2D model of the confined and saturated aquifer comprises an area of a square, the size of which has been defined in order to minimize the influence of the boundary conditions on the computational results, according to the results of the preliminary numerical study conducted in Section 3.6.3.

Namely, we consider a domain of size $14 \times 14\,\text{km}^2$ and an *active region* (with increased mesh resolution) of $6 \times 6\,\text{km}^2$, such that a distance of 4 km is assured between the active region and the boundary. The domain

Table 5 Mesh parameters used in the simulations

Modeling domain size	$14 \times 14\,\text{km}^2$
Subdomain with enhanced resolution	$6 \times 6\,\text{km}^2$
Smallest element diameter ($h_{\min}$)	$5.9\,\text{m}$
Largest element diameter ($h_{\max}$)	$281.8\,\text{m}$
# nodes of the spatial mesh	$547,200$
Time step length	3 months

is discretized with a non-uniform triangular mesh with characteristic mesh size of approximately 6 m in the *active region* (see Section 3.6.3). Outside the *active region*, the mesh is gradually coarsened, reaching a maximum element size of approximately 262 m near the boundary (see also Table 5).

It is worth noticing that the computational finite element mesh is generated only once at the beginning of the computational procedure and it is not updated at each optimization (when repositioning the wells). This aspect constitutes an important advantage of this numerical framework. Especially when computing numerous scenarios of multiple well configurations for a well placement optimization with finite element methods, computationally expensive and time-consuming re-meshing procedures would be otherwise required. The time discretization is chosen based on the simulation results described in Table 1, having a constant time step length $\Delta t = 3$ months.

4.4 Model parameters

We consider open hydraulic boundary conditions, i.e., we set boundary pressure in Eq. 3 as $P = 0\,\text{Pa}$, so that all pressure values are computed with respect to the pressure at the depth of the aquifer, where the reference (datum) is set.

For the energy balance Eq. 11, which describes the spatio-temporal evolution of the temperature field, we set initial and boundary conditions according to the depth of the aquifer and corresponding natural geothermal conditions in conduction-dominated hot sedimentary aquifers. Specifically, the boundary conditions for the temperature field are based on the initial temperature distribution that mimics a temperature gradient of approximately 30°C/km as described in Section 2.1. In particular, for the case of aquifers that extend horizontally, assuming a constant depth of approximately 3 km below surface and a surface temperature of 10°C, we set

$$
\begin{aligned}
T(0, \boldsymbol{x}) &= 100°\text{C}, \quad \text{for } \boldsymbol{x} \in \widehat{\boldsymbol{\Omega}}, \\
T(t, \boldsymbol{x}) &= 100°\text{C}, \quad \text{for } t > 0,\ \boldsymbol{x} \in \partial\widehat{\boldsymbol{\Omega}}.
\end{aligned} \tag{25}
$$

For the case of a dipping aquifer, we consider a temperature distribution that is constant in time and varies

in space linearly along the boundary, such that

$$
T(t, x, y) = \begin{cases} 100°\text{C}, & \text{for } x = 0\,\text{km}, \\ 130°\text{C}, & \text{for } x = 14\,\text{km}. \end{cases} \tag{26}
$$

Note that this corresponds to a difference in depth of about 1 km in the horizontal direction.

The parameters used in the numerical simulations are summarized in Table 6.

5 Simulation results

This section focuses on the numerical results obtained with the proposed computational framework.

The simulations have been performed solving the finite element problems defined by Eq. 13 and Eq. 16 with the open-source finite element library ParMooN [45], while the routines for the solution of the optimization problem related to the net energy Eq. 18 have been implemented using the open-source library NLopt[5] [104], which supports a large variety of derivative-free optimization algorithms.

The computational meshes have been generated using Gmsh [105], which is an open-source mesh generator[6]. For the visualization of the simulation results, the open-source post-processing tool ParaView [106] [7] has been employed.

5.1 Optimization parameters

In all the considered setups, we assume that the injection and production rates (Q_{inj}, Q_{prod}), the injection and production pressures (Δp^{inj}, Δp^{prod}), and the injection temperature T^{inj} do not depend on time. For each case, we performed 40 optimization steps and visualize the configuration of the optimization step that yielded the maximum net energy. If it is not explicitly stated otherwise, this will be the final optimization step. Let us note that an adequate number of optimization steps cannot be determined a priori in a theoretical manner. Instead, it has to be chosen heuristically in accordance with the time frame for the simulation and the desired accuracy of the result. In general, an increase of effort in the sense of more optimization steps has to be expected to enhance the optimality of the resulting controls. The choice of the number of optimization steps is particularly delicate if the behavior of the optimization functional (the objective function) cannot be classified as convex, having a global minimum, and/or being smooth.

The stopping criterion for the temperature simulation (in each optimization step) is twofold: On the one

---

[5]See https://nlopt.readthedocs.io.

[6]See www.gmsh.info.

[7]See www.paraview.org.

Table 6 Top table: Petrophysical properties of the reservoir rock, fluid mechanical properties, reservoir dimensional parameters, and operational parameters used in the simulations, partly taken from [18, 30]. Bottom table: Numerical parameters used in the simulations

Notation	Unit	Parameter Name	Lattice	Hexagon
$\mu_{\text{eff}} = \mu$	kg/m s	viscosities	0.0003	
$\mathbb{K}$	m^2	permeability	$\in 3 \cdot \{10^{-11}, 10^{-12}, 10^{-15}\}$	
H	m	aquifer thickness	300	
Q_{inj}, Q_{prod}	l/s	injection, production flow rates	100	$\in \{50, 100\}$
r_w	m	well radius	0.2	
t^L	yr	maximum lifetime	80	
ϕ	-	porosity	0.28	
ρ_f	kg/m^3	fluid/brine density	1050	
C_f	J/kg K	fluid/brine heat capacity	4200	
ρ_s	kg/m^3	rock density	2650	
C_s	J/kg K	rock heat capacity	730	
λ_s	J/K m s	thermal conductivity (rock)	2.7	
λ_f	J/K m s	thermal conductivity (fluid/brine)	0.7	
α_L	m	longitudinal dispersion coefficient	5	
α_T	m	transversal dispersion coefficient	0	
T_{inj}	K	injection temperature	$323.15\ (= 50\,^\circ C)$	
T_0	K	aquifer/formation temperature	$373.15\ (=100\,^\circ C)$/linear	
T_{quit}	K	minimum production temperature	$363.15\ (= 90\,^\circ C)/-10\%$	
ε	-	pump efficiency	0.6	
α	-	stabilization parameter (GLS)	1	
δ	-	stabilization parameter (grad-div)	0.1	
$\ell_{\boldsymbol{\Omega}}$	m	characteristic length	300	
γ	-	penalty for temperature BC	100	
r_ε	m	artificial well radius (IBM)	50	
N_O	-	optimization steps	40	

hand, the maximum production time is restricted to 80 years. On the other hand, the simulation stops whenever the specific lifetime is reached (see Section 3.3.2). The threshold temperature T_{quit} is defined based on a 10% temperature reduction with respect to the initial aquifer temperature. Due to the model approach (the non-matching immersed boundary method, see Section 3.4), the production temperatures at measurement points along the concentric circle of radius r_ε (enclosing the well) are utilized. For the sake of visibility of the active modeling domain defined in Subsection 3.6.3, the velocity, pressure, and temperature fields will be only shown within a centered $6 \times 6\,\text{km}^2$ subdomain, which is in line with the allowed variation in the control variables (lattice size/hexagon radius, translation, and rotation).

It is worth noting that for each configuration tested, the velocity and the pressure fields remain constant over the entire simulation time. This is the result of the assumptions made in the formulation of the physical problem.

Generally, the symbol $\oplus$ is utilized to refer to an injection well, while $\ominus$ represents a production well.

5.2 Lattice configurations

5.2.1 Optimal placement and net energy

In Fig. 15, we plot for each of the lattice scenarios introduced in Subsection 4.1 (see also Table 3) the resulting net energy over the optimization steps.

The results show the strong impact of the inter-well distance (lattice size) on the extracted energy. In fact, including the variation of the lattice size as optimization variable (setups LC and L1) allows to increase the obtained energy by approximately up to 300% with respect to the cases L2 and L3, where the lattice size is kept fixed.

The net energy for LC is generally smaller than that for L1, which can be explained by the larger average temperature of the considered aquifer domain in L1. The net energy for the setups with fixed lattice size (L2 and L3) is more robust with respect to a variation of their controls. In particular, the homogeneous setup L2 has an almost constant energy level which is larger than the slightly
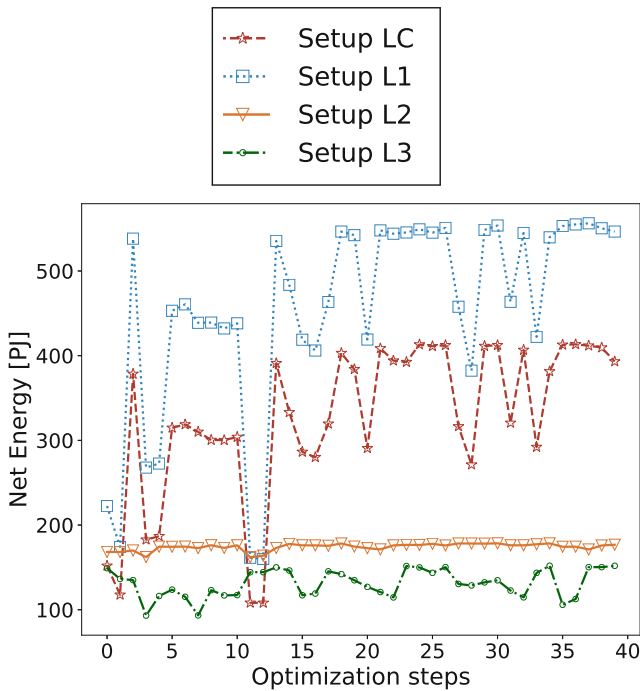
Fig. 15 Net energy for 40 optimization steps for the four different lattice scenarios (Table 3)

varying energy associated with its heterogeneous (with partly lower permeability) version L3.

Finally, the simulation results for the scenario L1 show that alone for a $6 \times 6\,\text{km}^2$ area covered with an optimized 4×4 doublet array structure operating with $100\,\text{l/s}$, around $219\,\text{MW}_{\text{th}}$ ($\approx 553\,\text{PJ}$ in 80 years operation time) can be developed for district heating. Concerning the planned heat contribution of $400\,\text{MW}_{\text{th}}$ from geothermal energy in the case of the city of Munich, this result suggests that such optimized doublet arrays are capable to reach this goal.

5.2.2 Simulation results in the optimal configurations

The optimization algorithm consists of simulating multiple scenarios using an appropriate sampling of the control variable space. Depending on the considered setup, the inter-well distance (lattice size), the translation in the direction of the x-axis, and the rotation angle have been varied automatically in order to detect the configuration that maximizes the net energy. All scenarios consider a doublet operational scheme with the parameters specified in Table 6.

In this section, computational results in the optimal geometrical configurations are analyzed with respect to the resulting velocity, pressure, and temperature fields, with the latter shown at the end of the lifetime as specified in Subsection 3.3.2. Detailed numerical results are shown only for selected cases (L1 and L3).
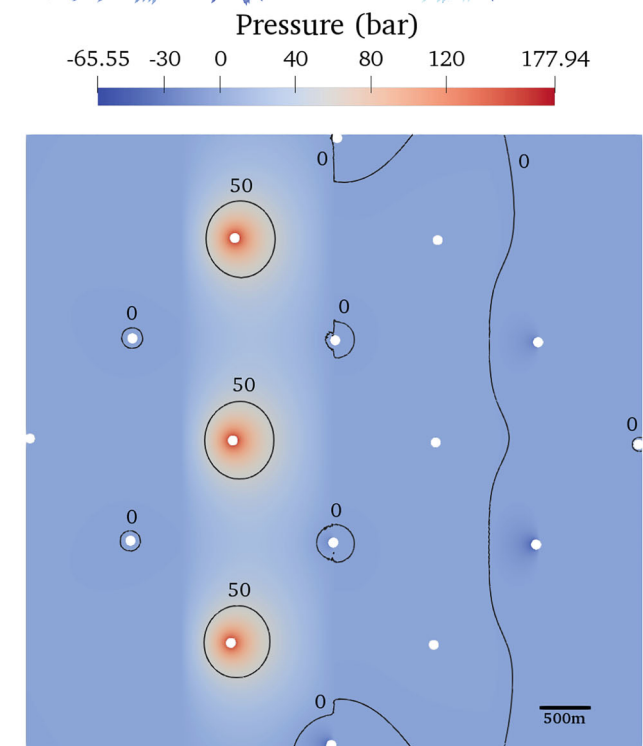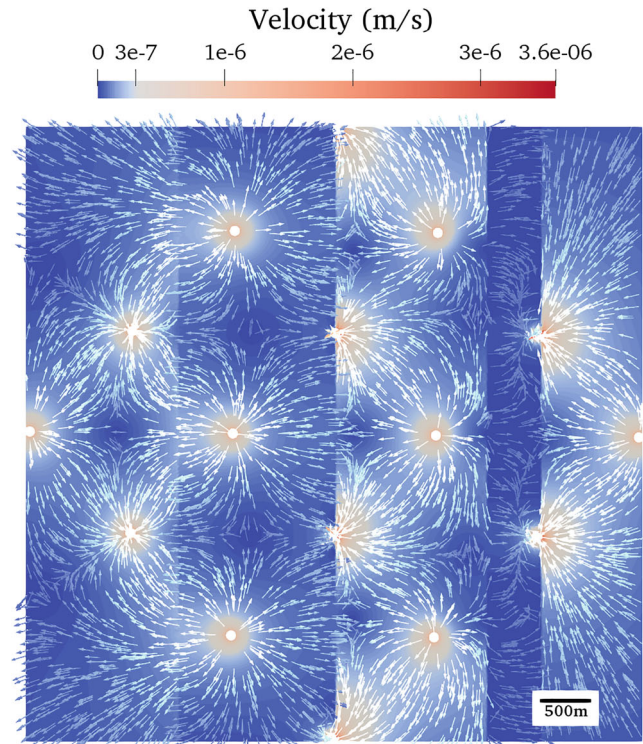
Fig. 16 Setup L1 in the optimal configuration (rotation angle = 2.35 rad, lattice size = 1397 m). Velocity field with unscaled arrows (top) and pressure field with selected contours (bottom)

Scenario L1 In this setting, a linearly varying initial temperature distribution is prescribed, as described in Subsection 4.4. The maximum net energy is obtained
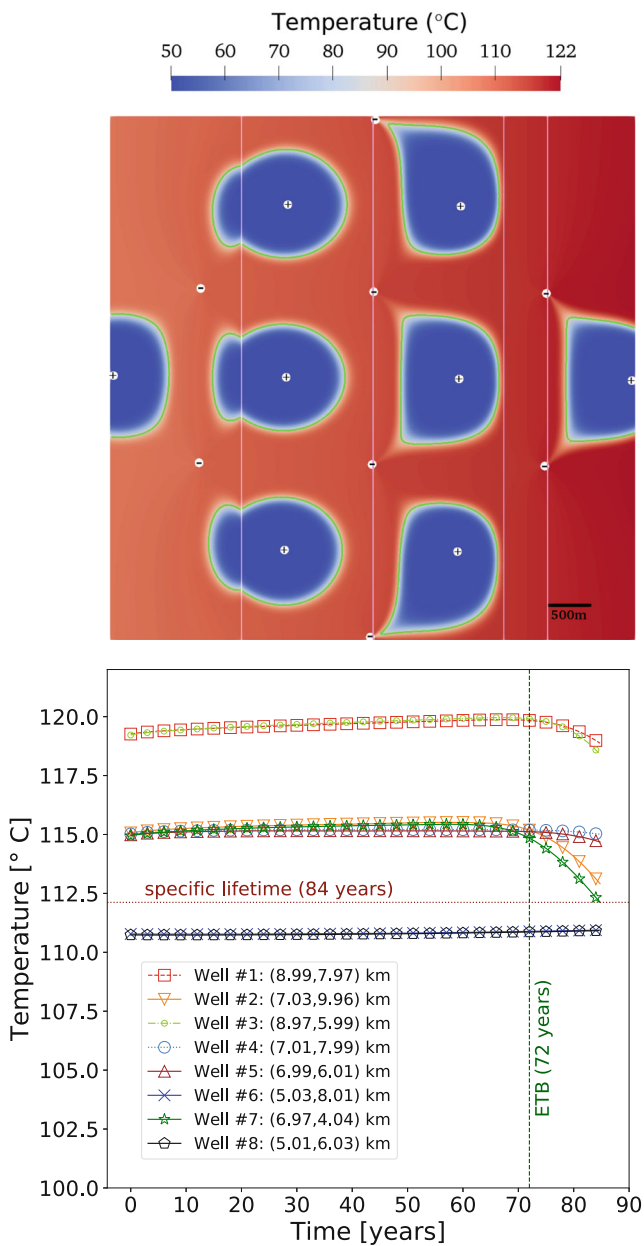
Fig. 17 Setup L1 in the optimal configuration (rotation angle = 2.35 rad, lattice size = 1397 m). Temperature distribution after 80 years of operation (top) with pink lines delimiting the different permeability regions and 90°C isolines depicted with a green line. Temperature evolution for each production well (bottom), showing the earliest thermal breakthrough (ETB). Note that the production temperature for the wells placed in the colder parts, instead of dropping, is initially increasing over time, due to fluid coming from hotter sections of the reservoir

at the optimization step 38. However, due to the (on average) higher reservoir temperature in comparison with the reservoir temperature set in the scenario LC, a higher
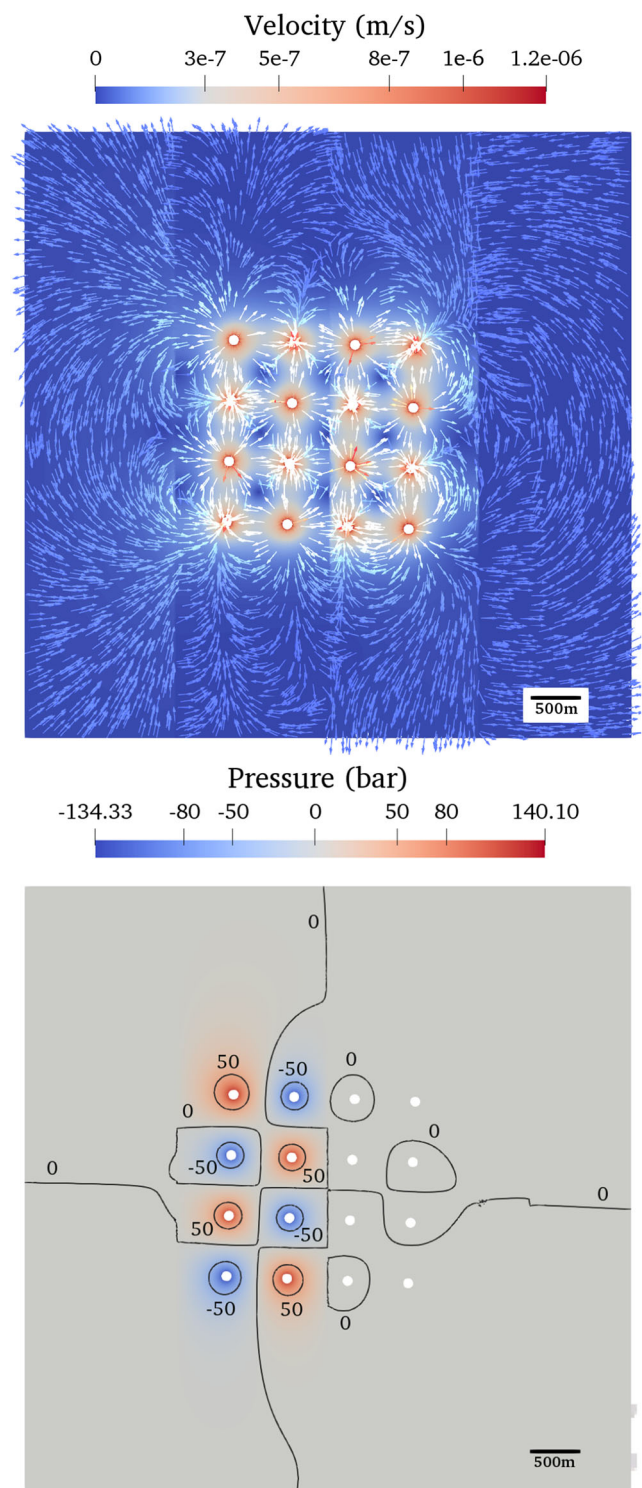
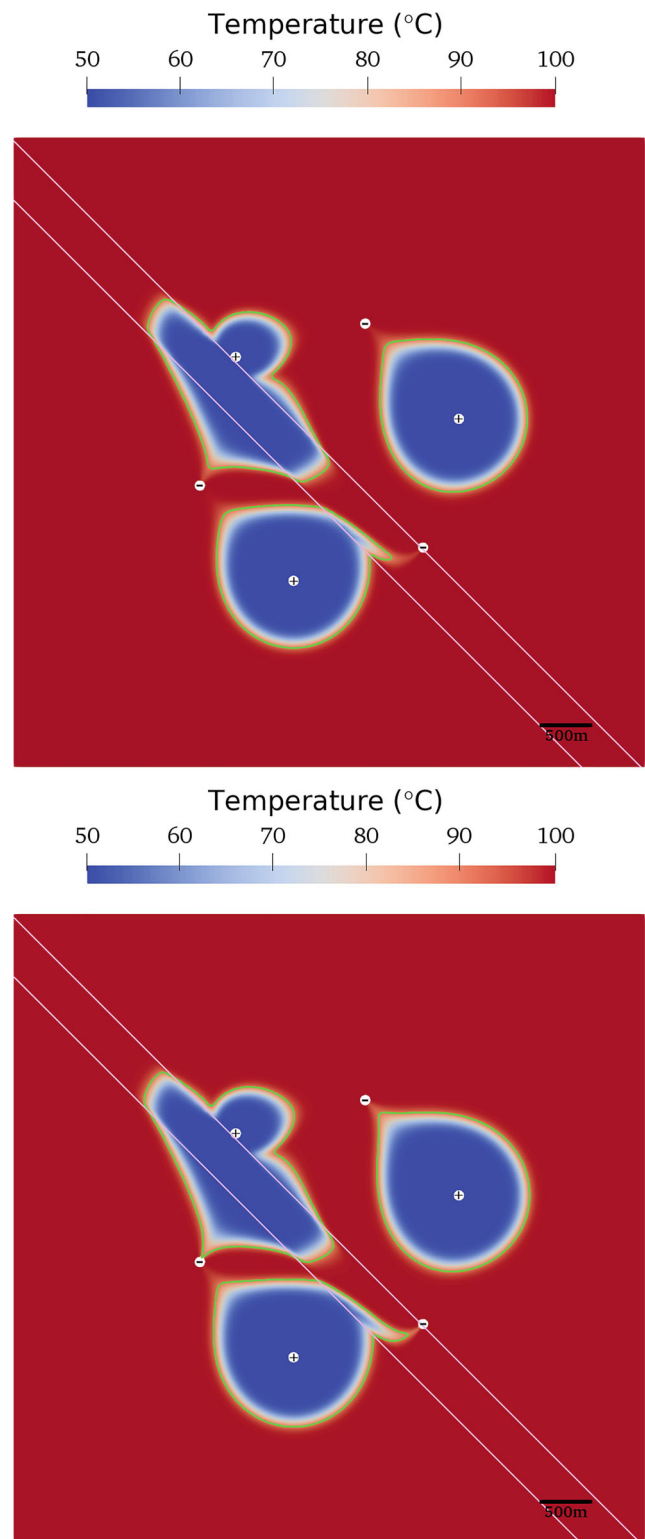**Fig. 18** Setup L3 in the optimal configuration (rotation angle = 1.53 rad, translation = −70.35 m). Velocity field with unscaled arrows (top) and pressure field with selected contours (bottom). Note in the pressure field (bottom) that half of the wells are situated outside the low permeability zones
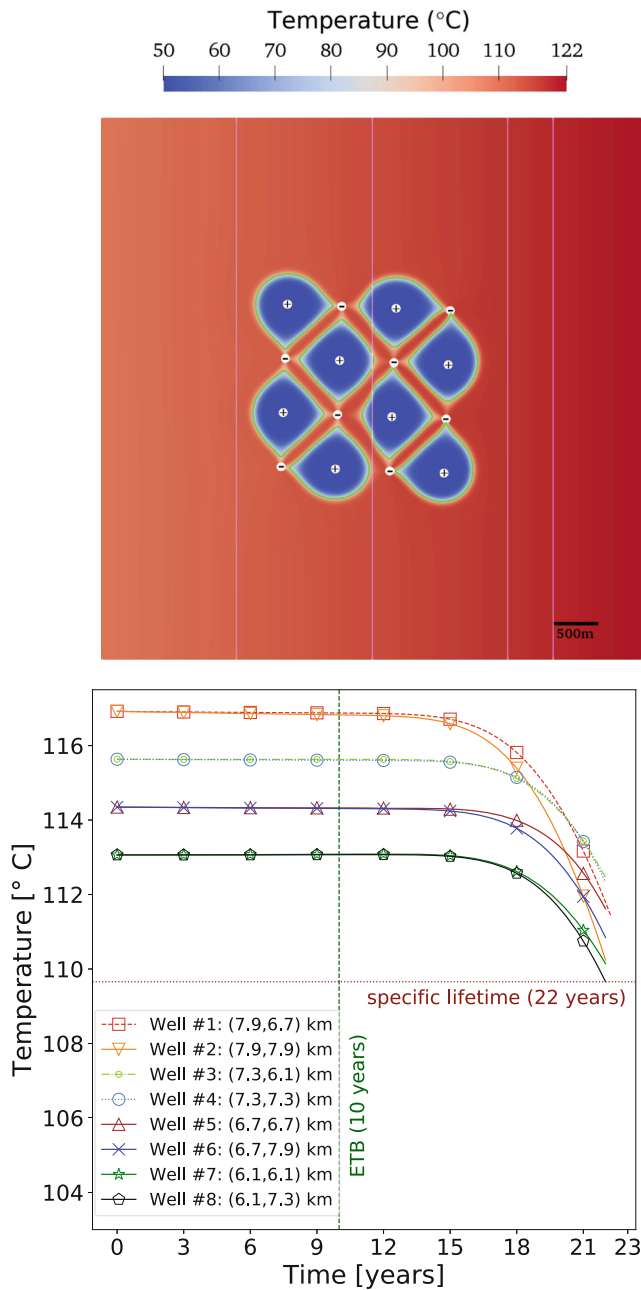
Fig. 19 Setup L3 in the optimal configuration (rotation angle = 1.53 rad, translation = −70.35 m). Temperature field at the specific lifetime of 22.75 years (top) with pink lines delimiting the different permeability regions and 90°C isolines depicted with a green line. Temperature evolution for each production well (bottom), showing the earliest thermal breakthrough (ETB). Note the different speeds of temperature drop of the respective production wells

Fig. 20 Setup $H_{(3,3)}$—Net energy (top), hexagon radius (middle), hexagon rotation angle (bottom) over 40 optimization steps for different damage zone widths

value of the net energy is obtained for this scenario (see Fig. 15). The optimal configuration is obtained with rotation angle = 2.35 rad and lattice size = 1397 m (translation is fixed to 0 m). The flow and the pressure fields are depicted in Fig. 16, while the temperature field after 80 years and the

temperature evolution at the production wells are depicted in Fig. 17.

For the allowed degrees of freedom of movement of the well positions and the considered heterogeneous structure of the aquifer, the computed optimal configuration suggests that a moderately linearly varying reservoir temperature has almost no impact on the optimization. In contrast, variations in the permeability of several orders of magnitudes as it is typical for carbonate reservoirs have a greater impact on the optimal placement of the wells in such doublet arrangements for a utilization time of 80 years.

According to the considered control variables, the optimal configuration is reached by accommodating the
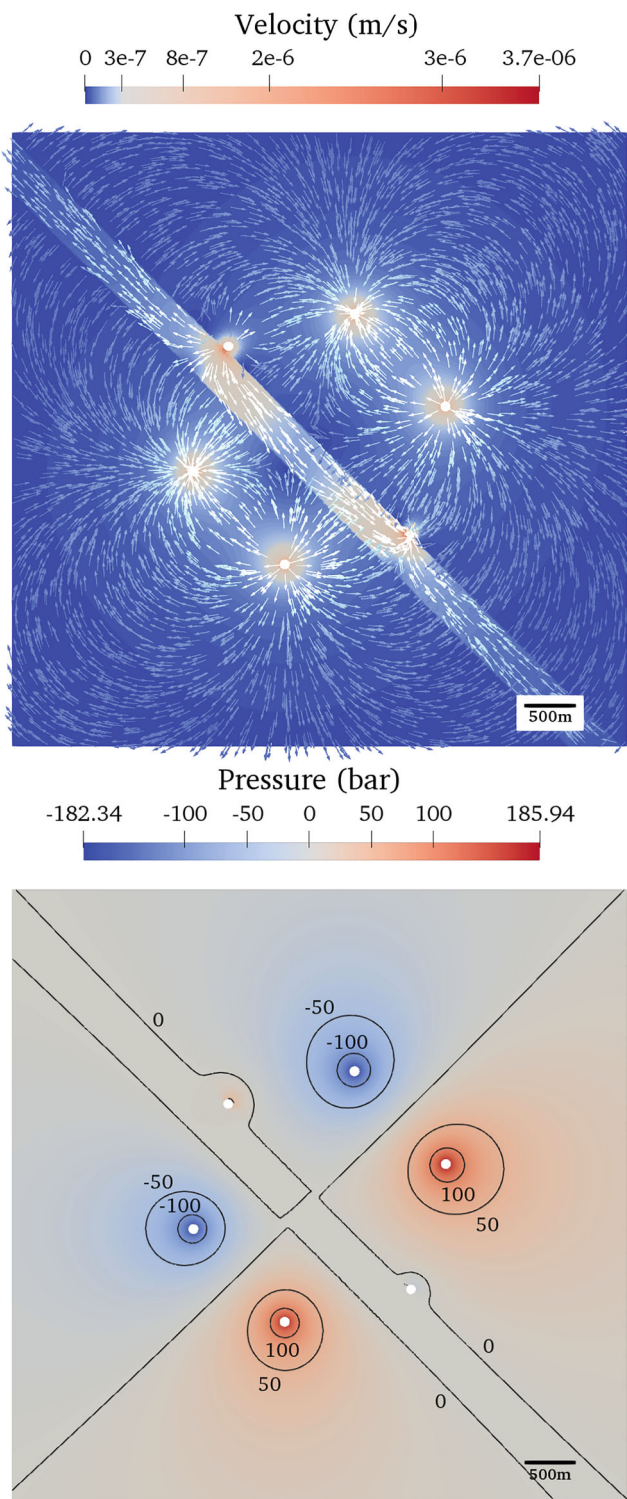
Fig. 21 Setup H(3,3) in the optimal configuration (rotation angle = 2.35 rad, hexagon radius = 1271 m). Velocity field with unscaled arrows (top) and pressure field with selected contours (bottom) for a fault damage zone width of 400 m
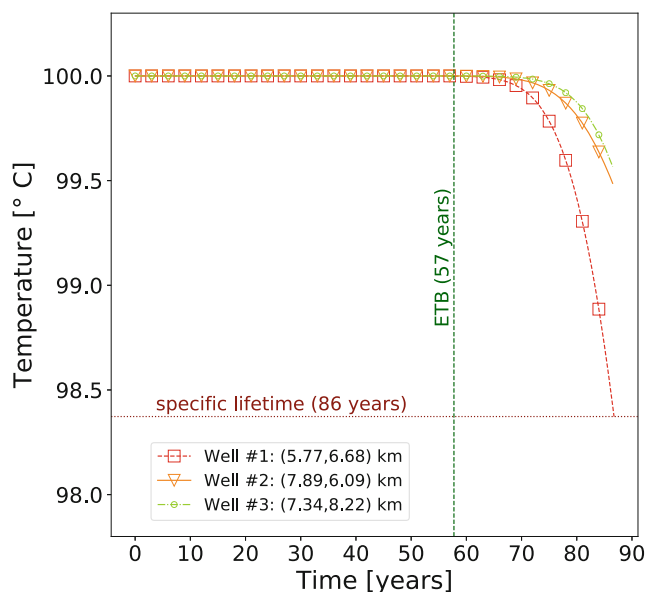

Fig. 22 Setup H(3,3) in the optimal configuration (rotation angle = 2.35 rad, hexagon radius = 1271 m). Temperature distribution after 80 years of operation (top) and at the end of the specific lifetime after 86.75 years of operation (bottom). A 90°C isoline is depicted with a green line. The pink lines delimit the different permeability regions

Fig. 23 Setup $H_{(3,3)}$ in the optimal configuration (rotation angle = 2.35 rad, hexagon radius = 1271 m). Temperature evolution for each production well, showing the earliest thermal breakthrough (ETB)

doublet lattice structure with a lattice size close to the maximum allowed, within an active modeling domain of $6 \times 6 \, \text{km}^2$.

In terms of pressure, the geothermal doublet lattice structure is rotated and the lattice size is adjusted, aiming at minimizing the pressure difference between injection and production wells, while striving for a well positioning that allows to maintain the aquifer temperature at the production wells as long as possible within the considered maximum time period of operation. This is manifested in Figs. 16 and 17 by placing less than half (only six) of the wells inside the low permeability zones.

As long as the thermal breakthrough does not occur within 80 years of operation (defined as the maximum operation time of the geothermal plant in this study), the placement of the wells in a heterogeneous permeability field is controlled mainly by the pressure difference between injectors and producers.

The lattice size is almost maximized with respect to the allowed range ([500, 1414] m). The heterogeneous permeability structure yields a reduced velocity in the low permeability regions, which decelerate the thermal breakthrough in one direction while accelerating it in another direction. Within the geometrical constraints imposed, three injection wells are placed entirely in the lower permeability regions, yielding to high pressures in order to realize the demanded flow rates. Translation of the lattice, which is not allowed in this case, or further enlarging the lattice beyond the chosen control range would allow to place less wells in the low permeability regions.

Similar results, concerning flow field and thermal breakthrough, were also obtained for the scenario LC, with the major difference that the maximum velocity reached in LC was around a factor 2.4 smaller compared with the scenario L1. This is caused by the placement of some wells directly at the boundary of the permeability contrast, leading to steeper pressure gradients in the immediate vicinity of the well.

Another important observation relates to the impact that the number of injection wells surrounding a production well has on the time of occurrence of the thermal breakthrough. We observe that the production wells located north and south are surrounded by the least number of injectors and undergo the earliest occurrence of the thermal breakthrough for the simulation time considered (see Fig. 17). In a regular lattice structure of doublet arrays, production wells located in the interior are surrounded by four injectors, whereas production wells located at the edges are surrounded by three or two injectors. Hence, an interior injection well distributes its induced flow rate to four surrounding production wells in different directions. That way the velocity of the fluid along each direct line connecting injection and production wells is lower than in the case of fewer surrounding production wells. Consequently, the progression of the cooling front emanating from the injection wells surrounded by the largest number of producers is slowed down, which is even promoted by unfavorable permeability structures. The hydraulic interaction between injectors and producers in combination with a heterogeneous permeability distribution explains the observation that those production wells, which fulfill both conditions, experience the earliest thermal breakthrough.

Scenario L3 In this configuration, in which translation and rotation of a regular lattice is allowed within a heterogeneous permeability structure and a linearly varying temperature distribution, the optimal configuration corresponds to the rotation angle = 1.53 rad and the translation = −70.35 m (lattice size is fixed to 600 m). The simulation results for this case are visualized in Figs. 18 and 19.

As can be seen in the velocity and pressure fields illustrated in Fig. 18, for the considered reservoir temperature variation, the optimal placement of the rigid lattice of doublets is mainly controlled by the permeability structure. For a fixed lattice size equal to 600 m and the considered degrees of freedom of movement (translation and rotation), the optimal configuration is reached by placing one-half of the lattice structure in a low permeability zone and the other half in a high permeability zone, where the latter has a higher average temperature. On the one hand, combining lower permeabilities with lower production temperatures for

half of the production wells allows to prolong the time of maximum production temperature at the expense of higher pressure. On the other hand, installing the other half in a higher permeability region with a higher average production temperature necessitates lower pressures at the price of an earlier thermal breakthrough (see Figs. 18 and 19). The permeability contrast between the lattice halves acts as a hydraulic barrier resulting in a deceleration of the cooling fronts evolution across the permeability contrast towards the zone of lower permeability.

The lateral temperature gradient in the order of magnitude considered in this study seems to have no significant impact on the translation of the lattice in the presence of the heterogeneous permeability structure with contrasts of several orders of magnitude.

The scenario L3 yields a much smaller specific lifetime of 22.75 years. A similar specific lifetime (24 years) was also obtained in the scenario L2. This is due to the fixed lattice size equal to 600 m and it is in line with the net energy results (see Fig. 15). In the previous scenario L1, the lattice size was allowed to vary and reached almost maximum permissible values, resulting in a much longer lifetime. This suggests that the inter-well distance predominantly controls the occurrence time of the thermal breakthrough and hence the economic lifetime of doublet geothermal facilities for the considered conditions.

From a more general point of view, the simulation results indicate that the pressure differences between injectors and producers generated by the combination of the flow rates imposed as exploitation strategy and the permeability structure have a stronger (negative) impact on the net energy compared with the temperature differences between injectors (fixed value) and producers generated by the considered lateral thermal gradient in reservoir.

5.3 Hexagon configurations

In this section, we present simulation results for five different scenarios in the case of a geothermal hexagonal multi-well structure (see Section 4.2 and Table 4). In all cases, initial and boundary aquifer temperatures are set to a constant value. Essentially, different operational strategies in a fault-controlled geothermal reservoir with varying damage zone width are examined in order to understand the impact that different operational schemes, hexagon geometrical parameters, and reservoir permeability structures considered have on the optimal configuration concerning the maximum net energy.

For all scenarios, we monitor the optimization activity via visualizing the net energy, the hexagon radius, and the hexagon rotation angle against the optimization step. In the following sections, detailed numerical results are presented for a selection of the considered setups (setups $H_{(3,3)}$,

$H_{(4,2)}$, and $H_{(2,4)}3$). Moreover, for the scenarios tested with varying damage zone width—$H_{(3,3)}$, $H_{(4,2)}$—only the results corresponding to the final/optimal positioning for a width of 400 m are presented. In terms of maximum net energy, this damage zone width is the most promising considered scenario. This is due to the fact that a larger subregion of the modeling domain has a higher permeability, which allows to place two wells partly inside the fault damage zone, such that on the one hand the pressure difference is smaller and on the other hand the progress of the cooling front is slower.

It is important to note that, except for the scenario $H_{(2,4)}2$, where the fault damage zone centrally passes through the center of the hexagon, the optimization is not able to place two wells entirely inside the damage zone. Further, for a decreasing damage zone width, the damage zone moves away from the center of the hexagon.

5.3.1 $H_{(3,3)}$—3 injection and 3 production wells

During the first optimization steps, we observe a strong variation of almost a factor 3 in the resulting net energy, see Fig. 20. The smallest values of the net energy correspond to small hexagon radii of less than 1 km. Hence, in this case, the inter-well distance has a much stronger impact on the net energy than the rotation angle, which is for all damage zone widths strongly varying until the end of the 40 optimization steps. For the hexagon radius, we observe structural repetitions, although the corresponding angles are changed. This may be related to the fact that for similar hexagon radii, different rotation angles of the hexagonal multi-well arrangement of alternated injectors and producers deliver similar values of net energy.

The final and optimal positioning is basically the same for the different damage zone widths; however, the largest considered damage zone of 400 m width yields the maximal net energy, which decreases with decreasing damage zone width.

Figures 21 and 22 illustrate the simulation results in terms of the velocity, pressure, and temperature fields for the optimal configuration.

The optimal placement of the wells is reached by deploying one injector and one producer in or as close as possible to the fault damage zone (at one border of the damage zone), which is a zone of enhanced permeability. This way the pressure difference between one injection and one production well is minimized, while the inter-well distance of this doublet is largest. In addition, the progress of the corresponding cooling front is channeled in the direction of the main axis of the fault damage zone and decelerated in the direction of the other neighboring production wells (see Fig. 22). Accordingly, the time of occurrence of the thermal breakthrough is substantially delayed and thus the specific lifetime prolonged (Fig. 23).
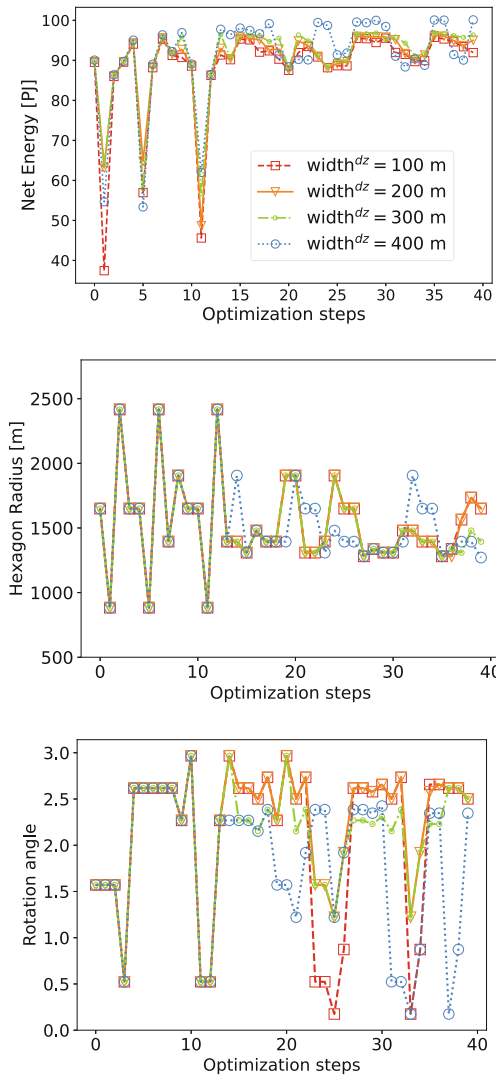
Fig. 24 Setup H$_{(4,2)}$—Net energy (top), hexagon radius (middle), and hexagon rotation angle (bottom) for 40 optimization steps for different damage zone widths
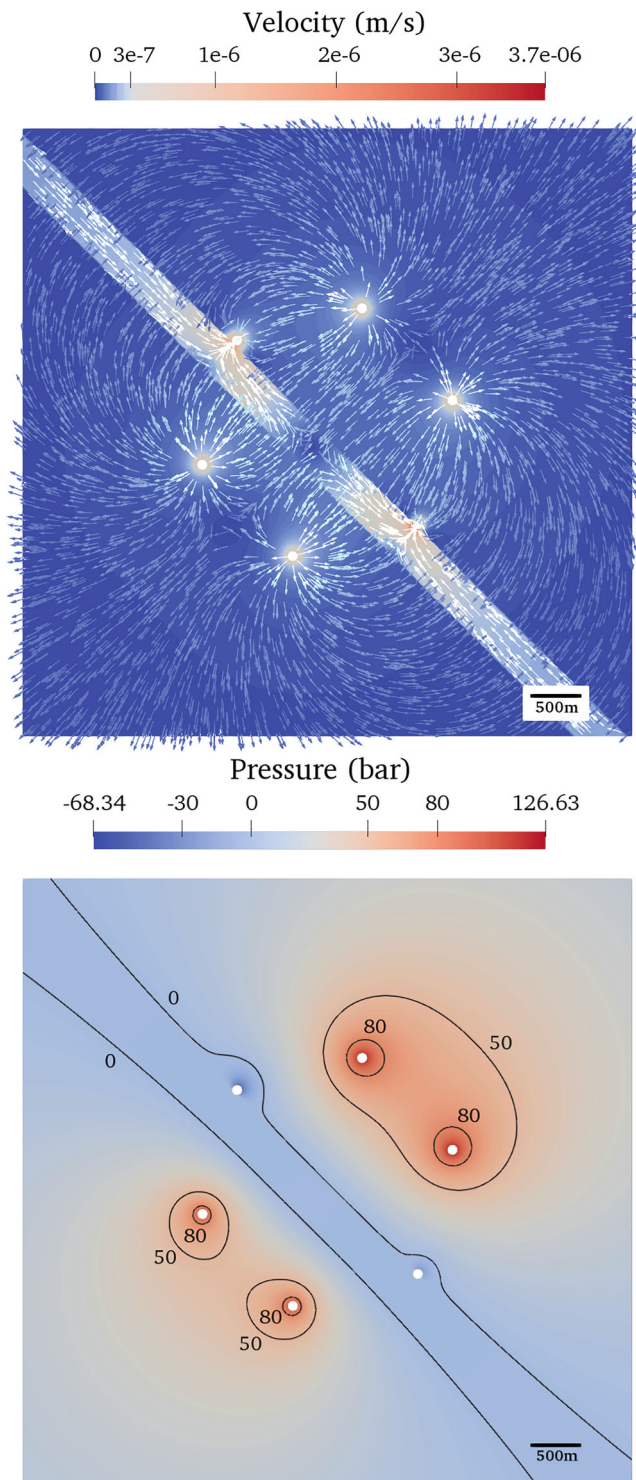

Fig. 25 Setup H$_{(4,2)}$ in the optimal configuration (rotation angle = 2.35 rad, hexagon radius = 1271 m). Velocity field with unscaled arrows (top) and pressure field with selected contours (bottom) for a damage zone width of 400 m

The specific lifetime for the final/optimal positioning of the wells occurs shortly after 80 years of operation. Another important observation relates to the thermo-hydraulic behavior of the two wells (doublet) placed at the farthest distance from the damage zone. The pressure and temperature fields of that doublet are not significantly influenced by the other wells such that the typical tear drop shape of the cooling front can be observed—similar to a single doublet simulation (see Fig. 13). Further, the temperature drops much faster at the production well situated at the westernmost corner of the multi-well hexagon than the other two production wells for the simulation time considered. As can be seen in the velocity field, in the vicinity of the wells partly situated inside the fault damage

zone we observe a predominantly linear flow behavior, whereas a bilinear flow is exhibited away from the wells at the extremes of the damage zone and matrix.
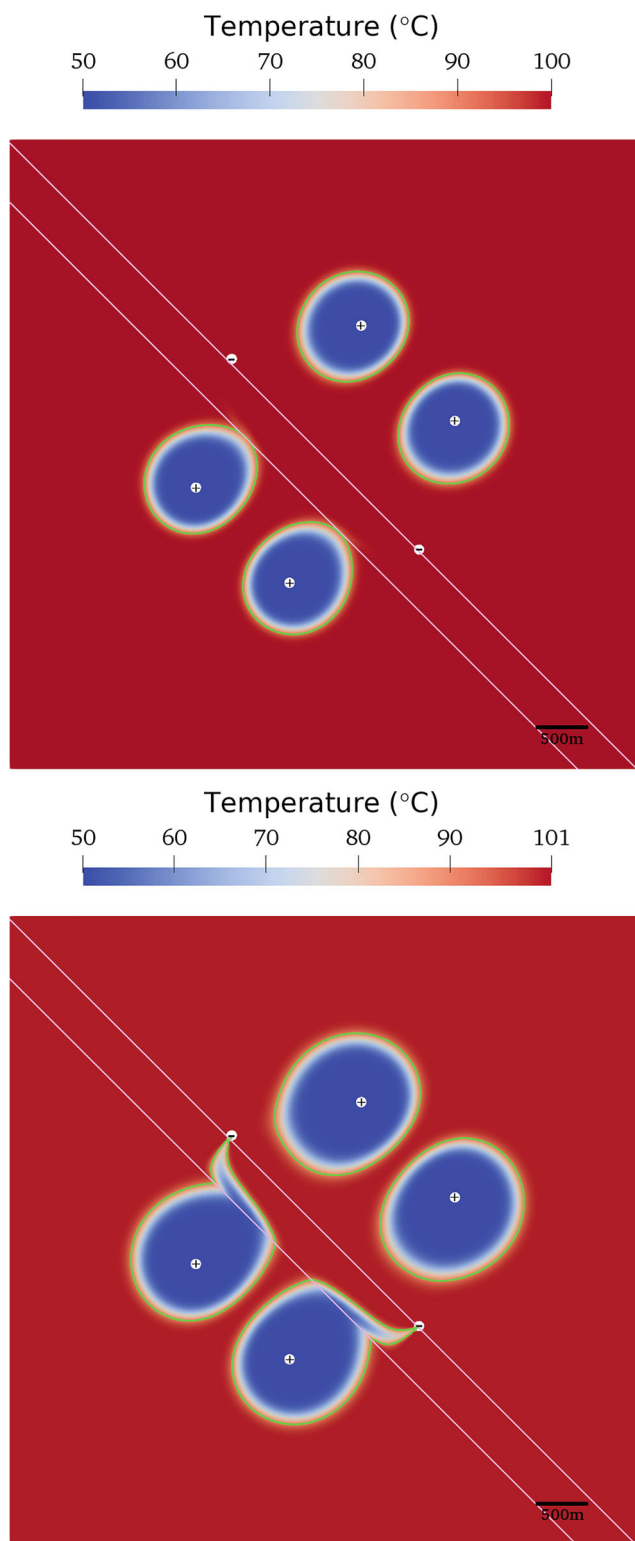
Temperature (°C)

Fig. 26 Setup H$_{(4,2)}$ in the optimal configuration (rotation angle = 2.35 rad, hexagon radius = 1271 m). Temperature distribution after 80 years of production (top) and at the end of the specific lifetime after 133.55 years of operation (bottom). The damage zone width is equal to 400 m. A 90°C isoline is depicted with a green line. The pink lines delimit the different permeability regions
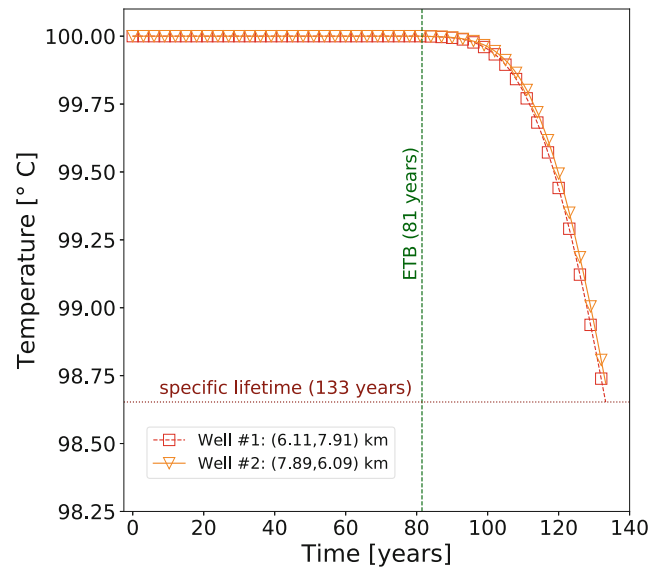

Fig. 27 Setup H$_{(4,2)}$ in the optimal configuration (rotation angle = 2.35 rad, hexagon radius = 1271 m). Temperature evolution at the production wells until the specific lifetime is reached, showing the earliest thermal breakthrough (ETB)

5.3.2 Setup H$_{(4,2)}$—4 injection and 2 production wells

Figure 24 compares the optimization processes for different widths of the fault damage zone. Similar as for the setup H$_{(3,3)}$, the damage zone width of 400 m yields the largest net energy. We also recognize a strong influence of the hexagon radius on the resulting net energy.

The resulting velocity and pressure fields for the optimal placement of the multi-well hexagonal configuration are displayed in Fig. 25.

In this setup, each production well has a twice as high flow rate as any injection well. The optimal configuration has been reached by placing the production wells as close as possible to the fault damage zone (around the border). As shown in Fig. 25 (top), the velocity field shows three different flow types (linear, bilinear, and radial) in the proximity of the wells in the fault damage zone and the matrix. In the vicinity of wells outside the fault damage zone, a radial flow behavior is observed. In the neighborhood of the production wells, a linear flow is established in the damage zone, whereas towards the center of the fault damage zone the flow gradually transforms into bilinear flow.

The placement of the wells with higher flow rates in or near the zone of higher permeability allows the pressure to diffuse with least resistance so that the pressure difference between injectors and producers is as low as possible. The temperature distribution after 80 years and at the end of the
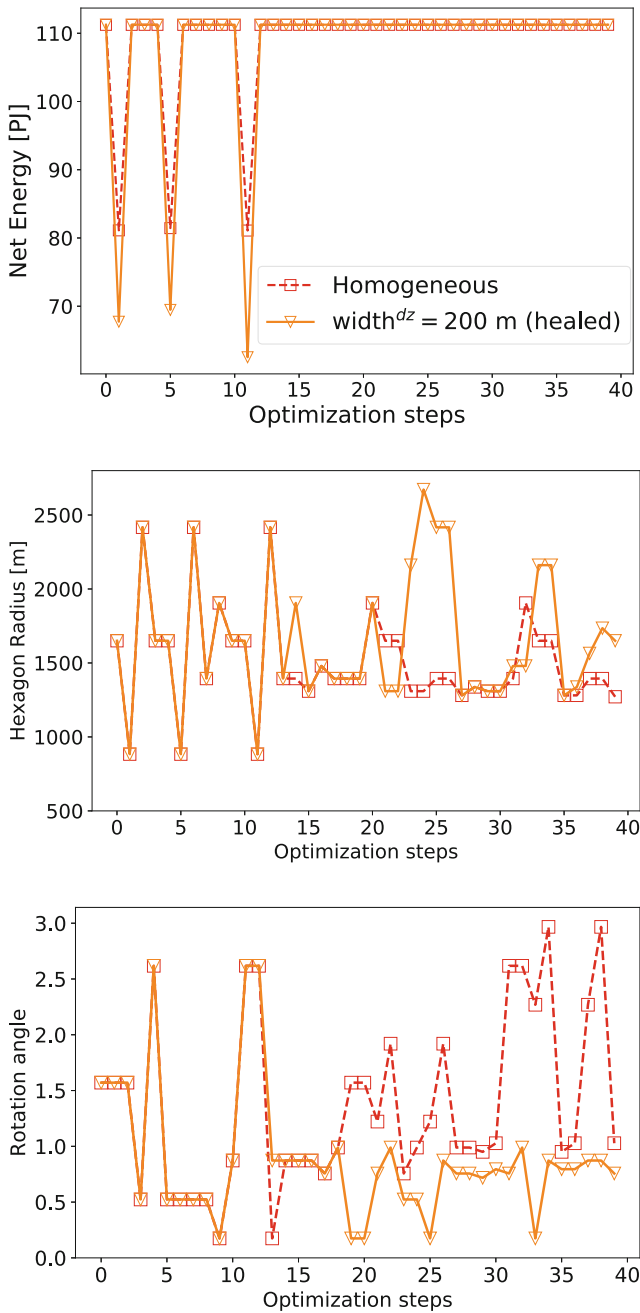
Fig. 28 Setup $H_{(2,4)}3$ versus homogeneous reservoir—Net energy (top), hexagon radius (middle), and hexagon rotation angle (bottom) during 40 optimization steps
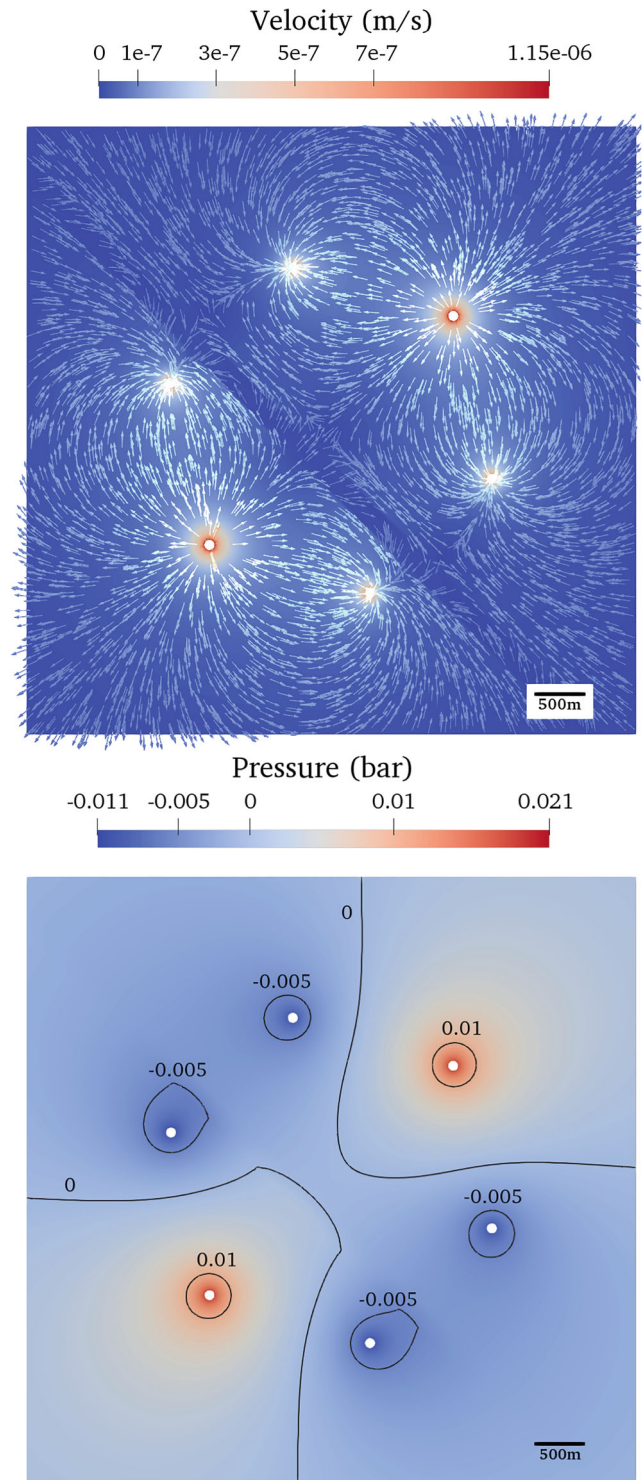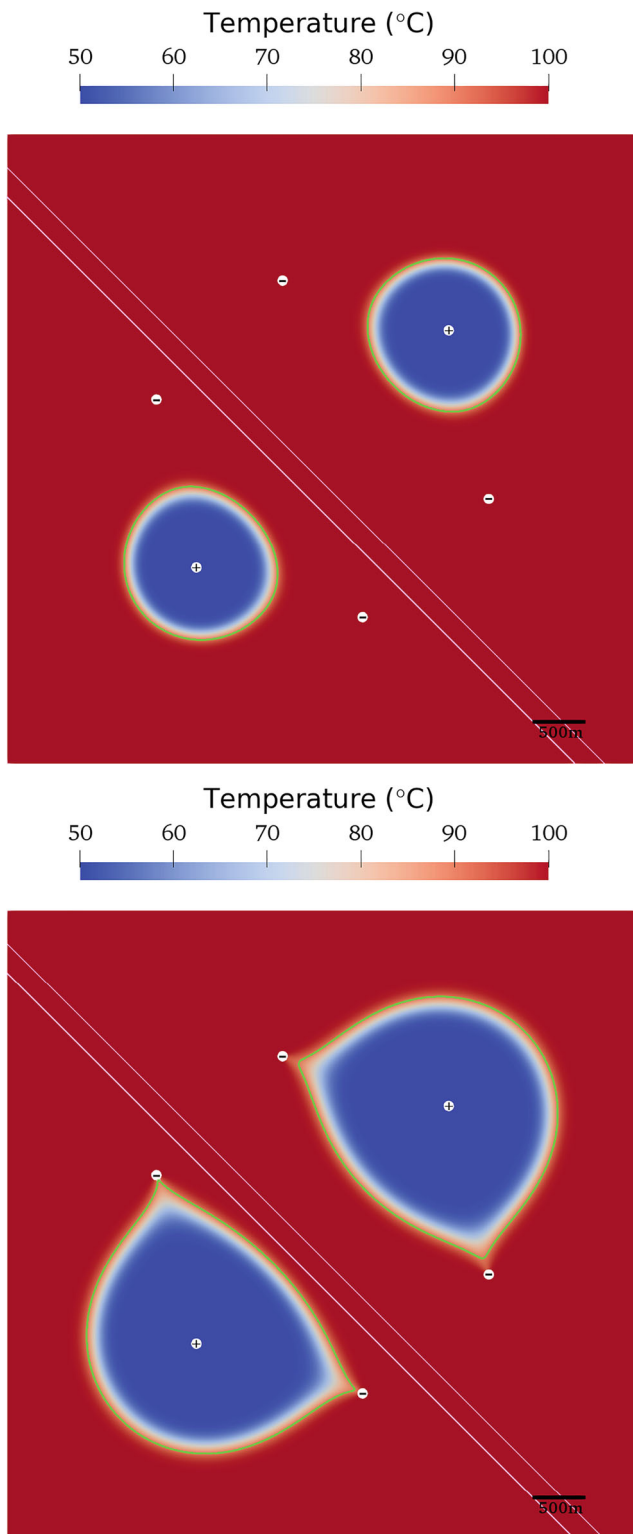

Fig. 29 Setup $H_{(2,4)}3$ in the optimal configuration (rotation angle $= 0.76$ rad, hexagon radius $= 1650$ m). Velocity field with unscaled arrows (top) and pressure field with selected contours (bottom) for the healed damage zone of width 200 m

specific lifetime of 133.55 years of operation are shown in Fig. 26.

Also the temperature fields reveal that placing the production wells as near as possible to the fault damage zone contributes to the deceleration of the cooling front from the injectors towards the producers. The cooling fronts develop essentially circular with a slight tendency towards the fault damage zone and reach the production wells almost simultaneously after 81 years (thermal breakthrough), by

passing along and through the high permeability region. The fact that the highest net energy is reached with the largest damage zone width reveals that although different
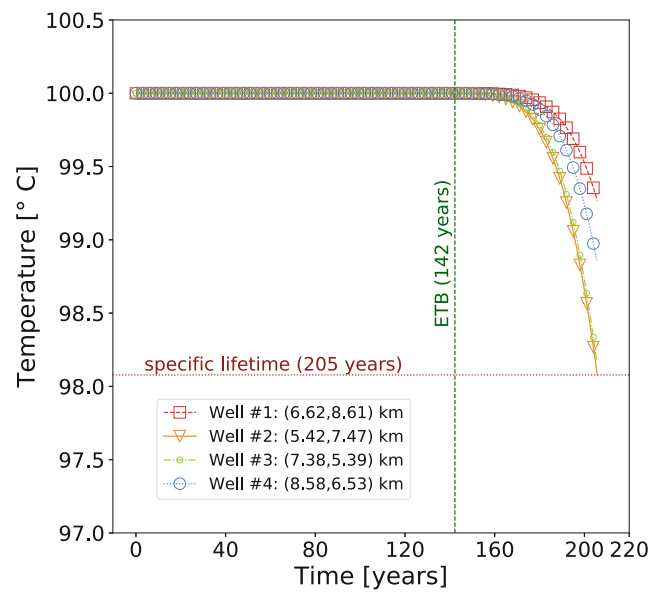
Temperature (°C)

Fig. 31 Setup $H_{(2,4)}3$ in the optimal configuration (rotation angle = 0.76 rad, hexagon radius = 1650 m). Temperature evolution for each production well for the healed damage zone of width 200 m

competing mechanisms at different stages of the thermo-hydraulic interaction between the wells are involved, placing the wells with highest flow rates as near as possible to the high permeable zone is decisive for the optimization of the net energy for the considered conditions.

The temperature evolution for the two production wells and the optimal positioning is displayed in Fig. 27. It reveals a symmetric character with respect to the fault damage zone, with a similar occurrence time of the thermal breakthroughs and speed of temperature decline for both production wells.

Further configurations considered (setups $H_{(2,4)}1$ and $H_{(2,4)}2$) corroborate the role of the maximum hexagonal radius as primary control on the net energy optimization. These setups comprise two injection wells with higher flow rates than the remaining four production wells. Similar to the setup $H_{(4,2)}$, placing the injection wells with higher flow rates in or as close as possible to the high permeability zone channels the cooling front along the fault damage zone and decelerates the progress of the cooling front in the direct line connecting injectors and producers. In doing so, the earliest thermal breakthrough time and the specific lifetime are significantly delayed. These optimal deployments also allow to reduce the pressure difference between injectors and producers the most.

5.3.3 Setup $H_{(2,4)}3$—2 injection and 4 production wells

The setup $H_{(2,4)}3$ considers a hexagon multi-well arrangement in a reservoir crossed by a fault damage zone with a

Fig. 30 Setup $H_{(2,4)}3$ in the optimal configuration (rotation angle = 0.76 rad, hexagon radius = 1650 m). Temperature distribution after 80 years of operation (top) and at the end of the specific lifetime after 205.75 years of operation (bottom). A healed damage zone of 200 m width is implemented. A 90°C isoline is depicted with a green line. The pink lines delimit the different permeability regions

relatively low healing capacity. The damage zone width is set to 200 m and the center of the hexagon does not coincide with the main axis of the fault damage zone. To better illustrate the simulation results, this setup is compared with the case of a hexagonal multi-well arrangement embedded in a reservoir with a homogeneous permeability distribution ($K = 3 \cdot 10^{-11} \, \mathrm{m^2}$). Figure 28 contrasts the optimization results for these two cases.

During the 40 optimization steps, the net energy behaves for both scenarios very similar and after an initial oscillating behavior it becomes almost constant. We observe also for these scenarios that small radii yield small net energies (optimization steps 2, 6, and 12, see Fig. 28). In the presence of a healed fault, this effect is even stronger due to reservoir compartmentalization. Notice that in this scenario the optimization excludes rotation angles of $\geqslant 1$ rad and thus the option to place the injection wells inside the healed fault, which would lead to higher pressure differences between injectors and producers but would also delay the thermal breakthroughs.

Figures 29 and 30 exhibit the velocity, pressure, and temperature fields for the optimal configuration of the hexagonal arrangement, respectively.

The optimal configuration is reached by placing a triplet on each side of the weakly healed fault, resulting in similar patterns for the velocity, pressure, and cooling front evolution in both sides of the reservoir with respect to the fault. The spatio-temporal evolution of the cooling fronts is similar to the case of the reservoir with homogeneous permeability. It is worth mentioning that the permeability contrast between the damage zone of 200 m width and the matrix is only one order of magnitude. Thus, a slight compartmentalization into two equally homogeneous reservoir sectors occurs.

Due to the initial geometrical configuration, one triplet is placed closer to the healed damage zone than the other triplet and both are slightly rotated with respect to the main axis of the fault damage zone. This explains the different temperature declines observed at the respective production wells in Fig. 31. The specific lifetime for this scenario is 205.75 years.

The physical plausibility of the simulation results in terms of the reached optimal deployment of geothermal multi-well systems in different reservoir structures and geothermal field development strategies corroborates the robustness of our proposed numerical framework.

6 Conclusions

We propose a computational framework for the modeling and simulation of coupled thermo-hydraulic reservoir processes in hot sedimentary aquifers, focusing on the optimization of smart multi-well systems for district heating. Our approach is based on coupled finite element methods for a generalized Darcy–Brinkman flow and for the heat advection. Geothermal wells are introduced using an immersed boundary approach that does not require the exact discretization of the well boundary within the computational mesh. The combination of two open-source solvers has been used to solve an optimization problem concerning geothermal energy production depending on the well position in heterogeneous reservoir conditions. In particular, we investigated the case of multi-well arrays in the form of a lattice and a hexagonal structure, considering structural and facies-related heterogeneities as well as varying reservoir temperatures, typically encountered in the Upper Jurassic (Malm) aquifer in the Greater Munich region. We focused on confined aquifers and reduced to two-dimensional domains. The extension to three dimensions requires a generalization of the non-matching immersed method for the wells, and will be tackled in upcoming work. Further aspects that will be object of future research include the utilization of gradient-based optimization methods and of model-order reduction techniques such as reduced basis or proper orthogonal decomposition methods.

Based on our numerical experiments, we conclude that significant amounts of energy can be generated by smart multi-well arrangements from hot sedimentary aquifers, potentially meeting the heat demand in densely populated cities as the city of Munich to a large extent. However, a detailed quantitative analysis is required for a sustainable and optimized reservoir development. Simulation results suggest that the complex thermo-hydraulic interaction between multiple wells and the heterogeneity of the reservoir rock permeability drive the optimal deployment of geothermal multi-well arrangements for the envisaged economic utilization time. Moreover, our computer experiments indicate that the combination of the developed numerical framework and multiple doublet arrays in a lattice structure is appropriate, on the one hand, for a comprehensive assessment of the extractable geothermal energy from deep geothermal reservoirs at a regional scale and, on the other hand, for the analysis of the impact of possible thermo-hydraulic interferences over a wide range of reservoir conditions and multi-well arrangements on the optimal net energy. Particularly, numerical simulations concerning multi-well hexagonal constellations placed around a fault damage zone reveal relevant thermo-hydraulic interactions in the optimal deployment, minimizing pressure difference between injectors and producers and maximizing thermal breakthrough occurrence time.

Our results show that an optimal positioning in heterogeneous reservoirs has a significant impact on the resulting net energy. Among the control variables, the distance

between the wells has influenced the objective function (the net energy) the most. The optimization processes evidence that within the imposed geometrical constraints, increasing the inter-well distance yields, on the one hand, a delayed thermal breakthrough time. On the other hand, it might allow to deploy multiple wells in more favorable permeability structures. In addition, the case of linearly varying reservoir temperature field could not be identified as significantly influencing the positioning of wells in the considered geological and geophysical settings.

From our simulations, we further conclude that the developed computational framework is especially suitable for the investigation of long-term geothermal reservoir performance affected by a large numbers of multi-well arrangements with placement optimization purposes. The implemented numerical method specifically facilitates the automatic search for the optimal deployment of smart multi-well arrangements, since it does not require to generate a new computational mesh when modifying the position of the wells. Modeling and simulation of coupled thermo-hydraulic reservoir processes resulting from the operation of diverse geothermal multi-well systems in numerous scenarios would otherwise be exceedingly time-consuming. Consequently, the methodology developed in this work may constitute an important tool in the large-scale development of hot sedimentary aquifers for district heating in urban regions worldwide.

References

1. Limberger, J., Boxem, T., Pluymaekers, M., Bruhn, D., Manzella, A., Calcagno, P., Beekman, F., Cloetingh, S., van Wees, J.-D.: Geothermal energy in deep aquifers: a global assessment of the resource base for direct heat utilization. Renew. Sustain. Energy Rev. **82**, 961–975 (2018)

2. Moeck, I.S.: Catalog of geothermal play types based on geologic controls. Renew. Sustain. Energy Rev. **37**, 867–882 (2014)

3. Bertani, R., Dumas, P., Bonafin, J., Flóvenz, O.G., Jónsdóttir, B., Manzella, A., Donato, A., Gola, G., Santilano, A., Trumpy, E., Simsek, S., van Wees, J.-D., Pluymaekers, M., Veldkamp, H., van Gessel, S., Bonté, D., Rybach, L., Sanner, B., Angelino, L.: Perspectives for Geothermal Energy in Europe. World Scientific Publishing Europe Ltd., New York (2017)

4. Ungemach, P., Antics, M.: Assessment of Deep Seated Geothermal Reservoirs in Selected European Sedimentary Environments. In: Proceedings of the World Geothermal Congress (2015)

5. Antics, M., Bertani, R., Sanner, B.: Summary of EGC 2016 Country Update Reports on Geothermal Energy in Europe. In: Proceedings of the European Geothermal Congress (2016)

6. Antics, M., Sanner, B.: Status of Geothermal Energy Use and Resources in Europe. In: Proceedings of the European Geothermal Congress (2007)

7. Hurter, S., Schellschmidt, R.: Atlas of geothermal resources in Europe. Geothermics **32**(4), 779–787 (2003)

8. Lund, J.W., Boyd, T.L.: Direct utilization of geothermal energy 2015 worldwide review. Geothermics **60**, 66–93 (2016)

9. Agemar, T., Alten, J.-A., Ganz, B., Kuder, J., Kühne, K., Schumacher, S., Schulz, R.: The Geothermal Information System for Germany - GeotIS. Zeitschrift der Deutschen Gesellschaft für Geowissenschaften **165**(2), 129–144 (2014)

10. Agemar, T., Weber, J., Schulz, R.: Deep geothermal energy production in Germany. Energies **7**(7), 4397–4416 (2014)

11. Dussel, M., Lüschen, E., Thomas, R., Agemar, T., Fritzer, T., Sieblitz, S., Huber, B., Birner, J., Schulz, R.: Forecast for thermal water use from Upper Jurassic carbonates in the Munich region (South German Molasse Basin). Geothermics **60**, 13–30 (2016)

12. Weber, J., Born, H., Moeck, I.: Geothermal Energy Use, Country Update for Germany 2016 - 2018. In: Proceedings of the European Geothermal Congress (2019)

13. Alten, J.-A., Thorsten, A., Gramenz, J., Tribbensee, M.: GeotIS: Free Access to Maps and 3D Models for Geothermal Project Planning in Germany. In: Proceedings of the European Geothermal Congress (2019)

14. Hecht, C., Pletl, C.: Das Verbundprojekt GRAME - Wegweiser für eine geothermische Wärmeversorgung urbaner Ballungsräume. Geothermische Energie, 82(2) (2015)

15. Buness, H., Von Hartmann, H., Lüschen, E., Meneses Rioseco, E., Wawerzinek, B., Ziesch, J., Thomas, R.: GeoParaMol: Eine Integration verschiedener Methoden zur Reduzierung des Fündigkeitsrisikos in der bayrischen Molasse. Geothermische Energie **85**, 22–23 (2016)

16. Meneses Rioseco, E., Ziesch, J., Wawerzinek, B., Von Hartmann, H., Thomas, R., Buness, H.: 3-D Geothermal Reservoir Modeling of the Upper Jurassic Carbonate Aquifer in the City of Munich (Germany) under the Thermal-Hydraulic Influence of Optimized Geothermal Multi-Well Patterns - Project GeoParaMol. In: Proceedings of the 43rd Workshop on Geothermal Reservoir Engineering (2018)

17. Meneses Rioseco, E., Ziesch, J., Von Hartmann, H., Buness, H.: Geothermal reservoir modelling and simulation of the Upper Jurassic aquifer for district heating in the city of Munich (Germany). In: Proceedings of the European Geothermal Congress (2019)

18. Willems, C.J.L., Nick, H.M., Weltje, G.J., Bruhn, D.F.: An evaluation of interferences in heat production from low enthalpy geothermal doublets systems. Energy **135**, 500–512 (2017)

19. Willems, C.J.L., Nick, H.M., Goense, T., Bruhn, D.F.: The impact of reduction of doublet well spacing on the net present

value and the life time of fluvial hot sedimentary aquifer doublets. Geothermics **68**, 54–66 (2017)

20. Park, H.-Y., Yang, C., Al-Aruri, A.D., Fjerstad, P.A.: Improved decision making with new efficient workflows for well placement optimization. J. Pet. Sci. Eng. **152**, 81–90 (2017)

21. Sayyafzadeh, M.: Reducing the computation time of well placement optimisation problems using self-adaptive metamodelling. J. Pet. Sci. Eng. **151**, 143–158 (2017)

22. Dossary, M.A.A., Nasrabadi, H.: Well placement optimization using imperialist competitive algorithm. J. Pet. Sci. Eng. **147**, 237–248 (2016)

23. Liu, D., Sun, J.: The Control Theory and Application for Well Pattern Optimization of Heterogeneous Sandstone Reservoirs. Petroleum Industry Press and Springer-Verlag, Berlin Heidelberg (2017). ISBN 978-3-662-53287-4

24. Li, T., Shiozawa, S., McClure, M.W.: Thermal breakthrough calculations to optimize design of a multiple-stage Enhanced Geothermal System. Geothermics **64**, 455–465 (2016)

25. Shook, G.M.: Predicting thermal breakthrough in heterogeneous media from tracer tests. Geothermics **30**(6), 573–589 (2001)

26. Blöcher, M.G., Zimmermann, G., Moeck, I., Brandt, W., Hassanzadegan, A., Magri, F.: 3D numerical modeling of hydrothermal processes during the lifetime of a deep geothermal reservoir. Geofluids **10**(3), 406–421 (2010). https://onlinelibrary. wiley.com/doi/pdf/10.1111/j.1468-8123.2010.00284.x

27. O'Sullivan, M.J., Pruess, K., Lippmann, M.J.: State of the art of geothermal reservoir simulation. Geothermics **30**(4), 395–429 (2001)

28. Bödvarsson, G.S., Tsang, C.F.: Injection and thermal breakthrough in fractured geothermal reservoirs. Journal of Geophysical Research: Solid Earth **87**(B2), 1031–1048 (1982). https://agupubs.onlinelibrary.wiley.com/doi/pdf/10.1029/ JB087iB02p01031

29. O'Sullivan, M.J.: Geothermal reservoir simulation. Int. J. Energy Res. **9**(3), 319–332 (1985). https://onlinelibrary.wiley.com/doi/ pdf/10.1002/er.4440090309

30. Crooijmans, R.A., Willems, C.J.L., Nick, H.M., Bruhn, D.F.: The influence of facies heterogeneity on the doublet performance in low-enthalpy geothermal sedimentary reservoirs. Geothermics **64**, 209–219 (2016)

31. Saeid, S., Al-Khoury, R., Nick, H.H.M., Barends, F.: Experimental-numerical study of heat flow in deep low-enthalpy geothermal conditions. Renew. Energy **62**, 716–730 (2014)

32. Saeid, S., Al-Khoury, R., Nick, H.H., Hicks, M.A.: A prototype design model for deep low-enthalpy hydrothermal systems. Renew. Energy **77**, 408–422 (2015)

33. Rostamian, A., Jamshidi, S., Zirbes, E.: The development of a novel multi-objective optimization framework for non-vertical well placement based on a modified non-dominated sorting genetic algorithm-II. Comput. Geosci. **23**, 1065–1085 (2019)

34. Zhang, L., Deng, Z., Zhang, K., Long, T., Desbordes, J., Sun, H., Yang, Y.: Well-placement optimization in an enhanced geothermal system based on the fracture continuum method and 0-1 programming. Energies **12**, 709 (2019)

35. Kahrobaei, S., Fonseca, R.M., Willems, C.J.L., Wilschut, F., van Wees, J.D.: Regional scale geothermal field development optimization under geological uncertainties. In: Proceedings of the European Geothermal Congress (2019)

36. McDonald, M.G., Harbaugh, A.W.: The history of MODFLOW. Ground Water **41**, 280–283 (2005)

37. Keilegavlen, E., Berge, R., Fumagalli, A., Starnoni, M., Stefansson, I., Varela, J., Berre, I.: Porepy: An open-source software for simulation of multiphysics processes in fractured porous media (2019)

38. Alnæs, M.S., Blechta, J., Hake, J., Johansson, A., Kehlet, B., Logg, A., Richardson, C., Ring, J., Rognes, M.E., Wells, G.N.: The FEniCS Project Version 1.5. Archive of Numerical Software **3**, 100 (2015)

39. Blatt, M., Burchardt, A., Dedner, A., Engwer, C., Fahlke, J., Flemisch, B., Gersbacher, C., Gräser, C., Gruber, F., Grüninger, C., Kempf, D., Klöfkorn, R., Malkmus, T., Müthing, S., Nolte, M., Piatkowski, M., Sander, O.: The distributed and unified numerics environment, version 2.4. Archive of Numerical Software **4**(100), 13–29 (2016)

40. Arndt, D., Bangerth, W., Clevenger, T.C., Davydov, D., Fehling, M., Garcia-Sanchez, D., Harper, G., Heister, T., Heltai, L., Kronbichler, M., Kynch, R.M., Maier, M., Pelteret, J.-P., Turcksin, B., Wells, D.: The deal.II library, version 9.1. J. Numer. Math. **27**, 203–213 (2019). accepted

41. Bilke, L., Flemisch, B., Kalbacher, T., Kolditz, O., Rainer, H., Nagel, T.: Development of open-source porous media simulators: principles and experiences. Transp. Porous Media **130**(1), 337–361 (2019)

42. Diersch, H.-J.G.: FEFLOW. Finite Element Modeling of Flow, Mass and Heat Transport in Porous and Fractured Media. Springer Science + Business Media; Springer Heidelberg Dordrecht, London (2014). ISBN 978-3-642-387388

43. Ghasemizadeh, R., Yu, X., Butscher, C., Hellweger, F., Padilla, I., Alshawabkeh, A.: Equivalent porous media (EPM) simulation of groundwater hydraulics and contaminant transport in karst aquifers. PLOS ONE **10**(9), 1–21 (2015)

44. Birner, J.: Hydrogeologisches Modell des Malmaquifers im Süddeutschen Molassebecken - Hydrogeological model of the Malm aquifer in the South German Molasse Basin. Ph.D. Thesis, Freie Universität Berlin (2013)

45. Wilbrandt, U., Bartsch, C., Ahmed, N., Alia, N., Anker, F., Blank, L., Caiazzo, A., Ganesan, S., Giere, S., Matthies, G., Meesala, R., Shamim, A., Venkatesan, J., John, V.: Parmoon – a modernized program package based on mapped finite elements. Comput. Math. Appl. **74**, 74–88 (2016)

46. Rybach, L.: Geothermal systems, conductive heat flow, geothermal anomalies. In: Geothermal Systems: Principles and case histories, pp. 3–31. John Wiley & Sons (1981)

47. Haenel, R., Rybach, L., Stegena, L. (eds.): Fundamentals of geothermics. Springer, Netherlands (1988)

48. Stober, I., Bucher, K.: Geothermal Energy. From Theoretical Models to Exploration and Development. Springer-Verlag, Berlin Heidelberg (2013). ISBN 978-3-642-13352-7

49. Ernst, H. (ed.): Geothermal Energy Systems: Exploration, Development, and Utilization. WILEY-VCH Verlag GmbH & Co. KGaA, Weinheim. ISBN 978-3-527-40831-3 (2010)

50. Förster, A., Merriam, D.F.: Geothermics in Basin Analysis, Computer Applications in the Earth Sciences. Springer US; Kluwer Academic/Plenum Publishers. ISBN 978-1-4613-7154-0 (1999)

51. Beardsmore, G.R., Cull, J.P.: Crustal Heat Flow: a Guide to Measurement and Modelling, Cambridge University Press (2001)

52. Haenel, R., Stegena, L., Rybach, L.: Handbook of Terrestrial Heat-Flow Density dDtermination: with Guidelines and Recommendations of the International Heat Flow Commission. Springer, Netherlands (2012)

53. Agemar, T., Schellschmidt, R., Schulz, R.: Subsurface temperature distribution in Germany. Geothermics **44**, 65–77 (2012)

54. Schütz, F., Winterleitner, G., Huenges, E.: Geothermal exploration in a sedimentary basin: new continuous temperature data and physical rock properties from northern Oman. Geothermal Energy **6**(1), 5 (2018)

55. Kukkonen, I.T., Jõeleht, A.: Weichselian temperatures from geothermal heat flow data. J. Geophys. Res. **108**, 2163, B3 (2003). https://doi.org/10.1029/2001JB001579

56. Förster, A.: Analysis of borehole temperature data in the Northeast German Basin: continuous logs versus bottom-hole temperatures. Pet. Geosci. **7**, 241–254 (2001)

57. Koch, A., Jorand, R., Vogt, C., Arnold, J.-C., Mottaghy, D., Pechnig, R., Clauser, C.: Erstellung statistisch abgesicherter termischer hydraulischer Gesteinseigenschaften für den flachen und tiefen Untergrund in Deutschland. Phase 2 - Westliches Nordrhein-Westfalen und bayerisches Molassebecken, RWTH Aachen (2009)

58. Fuchs, S., Förster, A.: Rock thermal conductivity of Mesozoic geothermal aquifers in the Northeast German Basin. Chemie der Erde – Geochemistry **70**, 13–22 (2010)

59. Clauser, C., Koch, A., Hartmann, A., Jorand, R., Rath, V., Wolf, A., Mottaghy, D., Pechnig, R.: Erstellung statistisch abgesicherter termischer hydraulischer Gesteinseigenschaften für den flachen und tiefen Untergrund in Deutschland. Phase 1 - Westliche Molasse und nördlich angrenzendes Süddeutsches Schichtstufenland, RWTH Aachen (2006)

60. Cermak, V., Huckenholz, H.-G., Rybach, L., Schmid, R., Schopper, J.-R., Schuch, M., Stöfler, D., Wohlenberg, J. In: Angenheister, G. (ed.): Physical Properties of Rocks, vol. 1a. Springer, Heidelberg (1982)

61. Sebastian, H., Götz, A.E., Sass, I.: Reservoir characterization of the Upper Jurassic geothermal target formations (Molasse Basin, Germany): role of thermofacies as exploration tool. Geothermal Energy Science **3**, 41–49 (2015)

62. Labus, M., Labus, K.: Thermal conductivity and diffusivity of fine-grained sedimentary rocks. J. Therm. Anal. Calorim. **132**(3), 1669–1676 (2018)

63. Clauser, C., Huenges, E.: Thermal Conductivity of Rocks and Minerals. In: Rock Physics & Phase Relations, pp. 105–126. American Geophysical Union (AGU) (2013)

64. Fuchs, S.: The variability of rock thermal properties in sedimentary basins and the impact on temperature modelling – a Danish example. Geothermics **76**, 1–14 (2018)

65. Mraz, E., Wolfgramm, M., Moeck, I., Thuro, K.: Detailed fluid inclusion and stable isotope analysis on deep carbonates from the North Alpine Foreland Basin to constrain paleofluid evolution. Geofluids **2019**, 23 (2019)

66. Jobmann, M., Schulz, R.: Hydrogeothermische Energiebilanz und Grundwasserhaushalt des Malmkarstes im süddeutschen Molassebecken, Niedersächsisches Landesamt für Bodenforschung. Archive Nr. 105040 (1989)

67. Dussel, M., Moeck, I., Wolfgramm, M., Straubinger, R.: Characterization of a Deep Fault Zone in Upper Jurassic Carbonates of the Northern Alpine Foreland Basin for Geotherma Production (South Germany). In: Proceedings of the 43rd Workshop on Geothermal Reservoir Engineering (2018)

68. Lüschen, E., Wolfgramm, M., Fritzer, T., Dussel, M., Thomas, R., Schulz, R.: 3D seismic survey explores geothermal targets for reservoir characterization at Unterhaching, Munich, Germany. Geothermics **50**, 167–179 (2014)

69. Haenel, R., Kleefeld, M., Koppe, I.: Geothermisches Energiepotential, Pilotstudie: Abschätzung der geothermischen Energievorräte an ausgewählten Beispielen in der Bundesrepublik Deutschland, Final report (Abschlussbericht), Bericht NLfB, Archive Nr. 96276, Bd. I-IV. Niedersächsisches Landesamt für Bodenforschung, Hannover, Germany (1984)

70. Haenel, R., Staroste, E.: Atlas of Geothermal Resources in the European Community, Austria and Switzerland, Niedersächsisches Landesamt für Bodenforschung, Hannover, Germany (1988)

71. Haenel, E.R. (ed.): The Urach geothermal project (Swabian Alb, Germany). Schweizerbart Science Publishers, Stuttgart, Germany (1982). ISBN 9783510651078

72. Hurter, S., Haenel, R.: Atlas of Geothermal Resources in Europe: Planning Exploration and Investments. In: Proceedings of the World Geothermal Congress (2000)

73. Majorowicz, J., Wybraniec, S.: New terrestrial heat flow map of Europe after regional paleoclimatic correction application. Int. J. Earth Sci. **100**(4), 881–887 (2011)

74. Cacace, M., Scheck-Wenderoth, M., Noack, V., Cherubini, Y., Schellschmidt, R.: Modelling the surface heat flow distribution in the area of Brandenburg (Northern Germany). Energy Procedia **40**, 545–553 (2013)

75. Noack, V., Cherubini, Y., Scheck-Wenderoth, M., Lewerenz, B., Höding, T., Simon, A., Moeck, I.: Assessment of the present-day thermal field (NE German Basin) – inferences from 3D modelling. Chemie der Erde – Geochemistry **70**, 47–62 (2010)

76. Fritzer, T.: Bayerischer Geothermieatlas - Hydrothermale Energiegewinnung: Technik, wirtschaftliche Aspekte, Risiken, hydrothermale Grundwasserleiter in Bayern, Untergrundtemperaturen in Bayern. Bayerisches Staatsministerium für Wirtschaft, Infrastruktur, Verkehr und Technologie, Munich (2010)

77. Agar, S.M., Geiger, S.: Fundamental controls on fluid flow in carbonates: current workflows to emerging technologies. Geol. Soc. Lond., Spec. Publ. **406**(1), 1–59 (2015). https://sp.lyellcollection.org/content/406/1/1.full.pdf

78. Agar, S.M., Hampson, G.J.: Fundamental controls on flow in carbonates: an introduction. Pet. Geosci. **20**(1), 3–5 (2014). https://pg.lyellcollection.org/content/20/1/3.full.pdf

79. Cacas, M.C., Daniel, J.M.: Nested geological modelling of naturally fractured reservoirs. Pet. Geosci. **7**(5), 43–52 (2001)

80. Beyer, D., Kunkel, C., Aehnelt, M., Pudlo, D., Voigt, T., Nover, G., Gaupp, R.: Influence of depositional environment and diagenesis on petrophysical properties of clastic sediments (Buntsandstein of the Thuringian Syncline, Central Germany). Zeitschrift der Deutschen Gesellschaft für Geowissenschaften **165**(3), 345–365 (2014)

81. Dethlefsen, F., Ebert, M., Dahmke, A.: A geological database for parameterization in numerical modeling of subsurface storage in northern Germany. Environmental Earth Sciences **71**(5), 2227–2244 (2014)

82. Kuder, J., Binot, F., Hübner, W., Orilski, J., Wonik, T., Schulz, R.: Für die Geothermie wichtige hydraulische Parameter von Gesteinen des Valangin und der Bückeberg-Formation (Wealden) in Nordwestdeutschland. Zeitschrift der Deutschen Gesellschaft für Geowissenschaften **165**(3), 455–467 (2014)

83. Kunkel, C., Aehnelt, M., Pudlo, D., Kukowski, N., Totsche, K.U., Gaupp, R.: Subsurface aquifer heterogeneities of Lower Triassic clastic sediments in central Germany. Mar. Pet. Geol. **97**, 209–222 (2018)

84. Olivarius, M., Weibel, R., Hjuler, M.L., Kristensen, L., Mathiesen, A., Nielsen, L.H., Kjøller, C.: Diagenetic effects on porosity-permeability relationships in red beds of the Lower Triassic Bunter Sandstone Formation in the North German Basin. Sediment. Geol. **321**, 139–153 (2015)

85. Stober, I.: Strömungsverhalten in Festgesteinsaquiferen mit Hilfe von Pump- und Injektionsversuchen. Schweizerbart Science Publishers, Stuttgart, Germany (1986)

86. Stober, I., Jodocy, M., Hintersberger, B.: Comparison of hydraulic conductivities determined with different methods in the Upper Jurassic of the southwest German Molasse Basin. Zeitschrift der Deutschen Gesellschaft für Geowissenschaften **164**(4), 663–679 (2013)

87. Ortiz Rojas, A.E., Dussel, M., Moeck, I.: Borehole geophysical characterisation of a major fault zone in the geothermal Unterhaching gt 2 well, South German Molasse Basin. Zeitschrift der

Deutschen Gesellschaft für Geowissenschaften **169**(3), 445–463 (2018)

88. Frisch, H., Huber, B.: Versuch einer Bilanzierung des Thermalwasservorkommens im Malmkarst des süddeutschen Molassebeckens. Hydrogeologie und Umwelt **20**, 25–43 (2000)

89. Brinkman, H.C.: A calculation of the viscous force exerted by a flowing fluid on a dense swarm of particles. Appl. Sci. Res. **1**(1), 27–34 (1949)

90. Popov, P., Efendiev, Y., Qin, G.: Multiscale modeling and simulations of flows in naturally fractured karst reservoirs. Commun. Comput. Phys. **6**(1), 162–184 (2009) MR2537310

91. Joodi, A., Sizaret, S., Binet, S., A., B., Albric, P., Lepiller, M.: Development of a Darcy-Brinkman model to simulate water flow and tracer transport in a heterogeneous karstic aquifer (Val d'Orl,ans, France). Hydrogeol. J. **18**, 295–309 (2009)

92. Willems, C.J.L., Goense, T., Nick, H.M., Bruhn, D.F.: The Relation Between Well Spacing and Net Present Value in Fluvial Hot Sedimentary Aquifer Geothermal Doublets: a West Netherlands Basin Case Study. In: Proceedings of the 41st Workshop on Geothermal Resevoir Engineering (2016)

93. Peskin, C.S.: The immersed boundary method. Acta Numerica **11**(1), 479–517 (2002)

94. D'Angelo, C.: Finite element approximation of elliptic problems with Dirac measure terms in weighted spaces: applications to one- and three-dimensional coupled problems. SIAM J. Numer. Anal. **50**(1), 194–215 (2012)

95. Cattaneo, L., Zunino, P.: A computational model of drug delivery through microcirculation to compare different tumor treatments. International Journal for Numerical Methods in Biomedical Engineering **30**(11), 1347–1371 (2014)

96. Scheidegger, A.E.: General theory of dispersion in porous media. Journal of Geophysical Research (1896-1977) **66**(10), 3273–3278 (1961), available at https://agupubs.onlinelibrary.wiley.com/doi/pdf/10.1029/JZ066i010p03273

97. Ciarlet, P.G.: The finite element method for elliptic problems. Classics in Applied Mathematics, vol. 40. Society for Industrial and Applied Mathematics (SIAM), Philadelphia, PA (2002)

98. Ern, A., Guermond, J.-L.: Theory and practice of finite elements. Applied Mathematical Sciences, vol. 159. Springer-Verlag, New York (2004)

99. Blank, L., Caiazzo, A., Chouly, F., Lozinski, A., Mura, J.: Analysis of a stabilized penalty-free Nitsche method for the Brinkman, Stokes, and Darcy problems. ESAIM: Mathematical Modeling and Numerical Analysis (M2AN) **52**(6), 2149–2185 (2018)

100. Gablonsky, J.M., Kelley, C.T.: A locally-biased form of the DIRECT algorithm. J. Global Optim. **21**(1), 27–37 (2001)

101. Ganesan, S., John, V., Matthies, G., Meesala, R., Shamim, A., Wilbrandt, U.: An Object Oriented Parallel Finite Element Scheme for Computations of PDEs: Design and Implementation. In: 2016 IEEE 23rd International Conference on High Performance Computing Workshops (HiPCW), pp. 106–115 (2016)

102. Llanos, E.M., Zarrouk, S.J., Hogarth, R.A.: Simulation of the Habanero Enhanced Geothermal System (EGS), Australia. In: Proceedings of the World Geothermal Congress (2015)

103. Vörös, R., Weidler, R., De Graaf, L., Wyborn, D.: Thermal modelling of long term circulation of multi-well development at the Cooper Basin hot fractured rock (HFR) project and current proposed scale-up program. In: Proceedings of the 32nd Workshop on Geothermal Reservoir Engineering (2007)

104. Johnson, S.G.: The NLopt nonlinear-optimization package. http://github.com/stevengj/nlopt

105. Geuzaine, C., Remacle, J.-F.: Gmsh: A 3-D finite element mesh generator with built-in pre- and post-processing facilities. Int. J. Numer. Methods Eng. **79**(11), 1309–1331 (2009)

106. Ahrens, J., Geveci, B., Law, C. In: Charles D. Hansen, Chris R. Johnson (eds.): 36-ParaView: An End-User Tool for Large Data Visualization. Visualization Handbook, pp. 717–731. Butterworth-Heinemann, Burlington (2005). isbn 978-0-12-387582-2

Affiliations

Laura Blank[1] · Ernesto Meneses Rioseco[2,3] · Alfonso Caiazzo[1] · Ulrich Wilbrandt[1]

Laura Blank
Laura.Blank@wias-berlin.de

Ernesto Meneses Rioseco
Ernesto.MenesesRioseco@leibniz-liag.de

Ulrich Wilbrandt
Ulrich.WIlbrandt@wias-berlin.de

[1] Weierstrass Institute for Applied Analysis and Stochastics (WIAS), Mohrenstrasse 39, 10117 Berlin, Germany

[2] Leibniz Institute for Applied Geophysics (LIAG), Stilleweg 2, 30655 Hannover, Germany

[3] Federal Institute for Geosciences and Natural Resources (BGR), Stilleweg 2, 30655 Hannover, Germany